

This work was written as part of one of the author's official duties as an Employee of the United States Government and is therefore a work of the United States Government. In accordance with 17 U.S.C. 105, no copyright protection is available for such works under U.S. Law.

Public Domain Mark 1.0

<https://creativecommons.org/publicdomain/mark/1.0/>

Access to this work was provided by the University of Maryland, Baltimore County (UMBC) ScholarWorks@UMBC digital repository on the Maryland Shared Open Access (MD-SOAR) platform.

**Please provide feedback**

Please support the ScholarWorks@UMBC repository by emailing [scholarworks-group@umbc.edu](mailto:scholarworks-group@umbc.edu) and telling us what having access to this work means to you and why it's important to you. Thank you.

## Wind Retrieval Algorithms for the IWRAP and HIWRAP Airborne Doppler Radars with Applications to Hurricanes

STEPHEN R. GUIMOND

*Earth System Science Interdisciplinary Center, University of Maryland, College Park, College Park, and  
NASA Goddard Space Flight Center, Greenbelt, Maryland*

LIN TIAN

*NASA Goddard Space Flight Center, Greenbelt, and Goddard Earth Sciences Technology and Research,  
Morgan State University, Baltimore, Maryland*

GERALD M. HEYMSFIELD

*NASA Goddard Space Flight Center, Greenbelt, Maryland*

STEPHEN J. FRASIER

*Microwave Remote Sensing Laboratory, University of Massachusetts Amherst, Amherst, Massachusetts*

(Manuscript received 26 June 2013, in final form 14 January 2014)

### ABSTRACT

Algorithms for the retrieval of atmospheric winds in precipitating systems from downward-pointing, conically scanning airborne Doppler radars are presented. The focus is on two radars: the Imaging Wind and Rain Airborne Profiler (IWRAP) and the High-Altitude IWRAP (HIWRAP). The IWRAP is a dual-frequency (C and Ku bands), multibeam (incidence angles of  $30^{\circ}$ – $50^{\circ}$ ) system that flies on the NOAA WP-3D aircraft at altitudes of 2–4 km. The HIWRAP is a dual-frequency (Ku and Ka bands), dual-beam (incidence angles of  $30^{\circ}$  and  $40^{\circ}$ ) system that flies on the NASA Global Hawk aircraft at altitudes of 18–20 km.

Retrievals of the three Cartesian wind components over the entire radar sampling volume are described, which can be determined using either a traditional least squares or variational solution procedure. The random errors in the retrievals due to the airborne radar geometry and noise in the Doppler velocities are evaluated using both an error propagation analysis with least squares theory and a numerical simulation of a hurricane. These analyses show that the vertical and along-track wind errors have strong across-track dependence with values ranging from  $0.25 \text{ m s}^{-1}$  at nadir to  $2.0$  and  $1.0 \text{ m s}^{-1}$  at the swath edges, respectively. The average across-track wind errors are  $\sim 2.5 \text{ m s}^{-1}$  or 7% of the hurricane wind speed. For typical rotated figure-four flight patterns through hurricanes, the zonal and meridional wind speed errors are  $\sim 1.5$ – $2.0 \text{ m s}^{-1}$ . Evaluations of both retrieval methods show that the variational procedure is generally preferable to the least squares procedure.

Examples of measured data retrievals from IWRAP during an eyewall replacement cycle in Hurricane Isabel (2003) and from HIWRAP during the development of Tropical Storm Matthew (2010) are shown. Comparisons of IWRAP-measured data retrievals at nadir to flight-level data show errors of  $\sim 2.0 \text{ m s}^{-1}$  for vertical winds and  $\sim 4.0 \text{ m s}^{-1}$  for horizontal wind speed ( $\sim 7\%$  of the hurricane wind speed). Additional sources of error, such as hydrometeor fall speed uncertainties and a small height offset in the comparisons, are likely responsible for the larger vertical wind errors when compared to the simulated error analyses.

### 1. Introduction

Knowledge of the three-dimensional distribution of winds in precipitating storm systems is crucial for

understanding their dynamics and predicting their evolution. The horizontal components of the wind contain the vast majority of the kinetic energy integrated over these systems and are responsible for structural damage to buildings and homes as well as providing energy input to the ocean. The vertical component of the wind is the heart of the precipitating storm system, playing a key

---

*Corresponding author address:* Stephen R. Guimond, NASA Goddard Space Flight Center, Code 612, Greenbelt, MD 20771.  
E-mail: stephen.guimond@nasa.gov

role in the formation of precipitation and the release of latent heat, which drives the dynamics. For those systems that spend the majority of their lifetime over ocean, such as tropical cyclones (TCs; our focus in this paper), airborne Doppler radar is the primary tool used to measure and calculate the three-dimensional winds.

There are several different airborne Doppler radar platforms used for TC research and operations. The X-band tail (TA) Doppler radar on the National Oceanic and Atmospheric Administration (NOAA) WP-3D aircraft scans in a plane perpendicular to the aircraft with the antenna typically alternating fore/aft, yielding along-track sampling of  $\sim 1.50$  km with 0.15-km gate spacing (Gamache et al. 1995). Another X-band radar system operated by National Center for Atmospheric Research (NCAR) called Electra Doppler Radar (ELDORA) has a similar scanning geometry to the NOAA radar with the exception of a faster antenna rotation rate providing along-track sampling of  $\sim 0.40$  km with 0.15-km gate spacing (Hildebrand et al. 1996). A National Aeronautics and Space Administration (NASA) X-band radar system called the ER-2 Doppler radar (EDOP), that flies on the ER-2 aircraft, has two fixed antennae, one pointing  $33^\circ$  forward and the other pointing at nadir, providing  $\sim 0.10$ -km along-track sampling and 0.04-km gate spacing (Heymsfield et al. 1996).

Doppler radars measure only the velocity of precipitation particles in the along-beam (radial relative to the radar) direction and thus retrieval algorithms are necessary to compute the three-dimensional winds. There are several methods for retrieving wind fields from airborne Doppler radars. One of the earliest techniques used was to fly two radar-equipped aircraft with orthogonal legs, which allows for the calculation of the horizontal wind components by interpolating the radial velocities to common grid points and solving the Doppler velocity projection equations (e.g., Marks and Houze 1984). Using methods of this type, the vertical wind can be estimated by using the computed horizontal winds to integrate the anelastic mass continuity equation in the vertical with appropriate boundary conditions (e.g., Bohne and Srivastava 1976; Ray et al. 1980; Marks et al. 1992).

A more modern technique for computing the three components of the wind from scanning airborne Doppler radars (NOAA TA and ELDORA) involves solving an optimization problem by minimizing a cost function that contains terms describing the misfit between modeled and observed radial velocities and possibly dynamical constraints on the wind field (e.g., Ziegler 1978; Chong and Campos 1996; Gao et al. 1999; Reasor et al. 2009; López-Carrillo and Raymond 2011; Bell et al. 2012). Two advantages of using this technique over the older methods described above are 1) improved accuracy of the

vertical wind component by eliminating the explicit integration of the anelastic mass continuity equation (Gao et al. 1999) and 2) the ability to incorporate additional data and/or dynamic constraints (such as the vertical vorticity equation; Shapiro et al. 2009) to improve the solution for the wind field. Even though the accuracy of the vertical wind has been improved using this method, significant errors are still possible (Matejka and Bartels 1998).

Last, a method for computing two components of the wind from scanning airborne radars in the nadir (and/or zenith) plane is to combine only the antenna positions forward and aft of the aircraft, which yields exact expressions for the vertical and along-track velocity. This is a unique situation of the common planes (COPLAN) method (Armijo 1969; Lhermitte 1970) utilized by the NASA EDOP radar. As with every wind retrieval technique, there are positive and negative attributes of this method. The main advantages are 1) highly accurate vertical and along-track winds due to the ability to form exact expressions for these components and 2) higher-horizontal-resolution grids (grid spacing typically equal to the along-track sampling) compared to other methods because only two radar views are necessary to compute the winds. The drawbacks of this method are the inability to retrieve all three Cartesian wind components, as retrievals are only possible in a two-dimensional plane along the aircraft track. In addition, for flight tracks not aligned along a cardinal direction or radial from a TC center, the interpretation of the along-track wind component for hurricane dynamics research is complicated.

The purpose of this paper is to describe wind retrieval algorithms that have been developed for a relatively new class of remote sensing instrument for TC studies: the downward-pointing, conically scanning airborne Doppler radar. One of these radars, the Imaging Wind and Rain Airborne Profiler (IWRAP) has been operating on the NOAA WP-3D aircraft since 2002, collecting data from storm systems in a wide variety of intensity stages (e.g., Fernandez et al. 2005). The other radar, the High-Altitude Imaging Wind and Rain Airborne Profiler (HIWRAP), is new and flew on the Global Hawk (GH) unmanned aircraft for the first time in 2010 during a NASA hurricane field experiment called Genesis and Rapid Intensification Processes (GRIP; Braun et al. 2013). An additional motivation for this paper is to briefly illustrate the TC science capabilities of both IWRAP and HIWRAP. The novelty of this study is in the application and understanding of the wind retrieval algorithms to the IWRAP/HIWRAP class of airborne radars as well as the detailed uncertainty analysis.

The paper is organized as follows: Section 2 introduces IWRAP and HIWRAP and presents wind

retrieval algorithms tailored to the unique scanning geometry of these radars. In addition, an error propagation analysis with least squares theory is derived for one of these retrieval algorithms. Section 3 presents the error characteristics of the wind retrieval algorithms using a realistic numerical simulation of a hurricane. Section 4 shows examples of IWRAP and HIWRAP wind retrievals from measured TC data. Finally, a summary of the paper and conclusions are presented in section 5.

## 2. Wind retrieval algorithms

### a. Description of IWRAP and HIWRAP

The IWRAP airborne Doppler radar was developed at the University of Massachusetts Amherst Microwave Remote Sensing Laboratory (UMASS MiRSL) with the intention of studying high-wind-speed regions of intense atmospheric vortices, such as hurricanes and winter storms. IWRAP is a dual-frequency (C and Ku bands), dual-polarized [horizontal/vertical (H/V)], downward-pointing, and conically scanning (60 rpm) Doppler radar with up to four beams between  $\sim 30^\circ$  and  $50^\circ$  incidence and 30-m range resolution. Typically, only two incidence angles are used for wind retrievals. Figure 1a shows the scanning geometry of IWRAP flying aboard the NOAA WP-3D aircraft, which has a typical flight altitude of  $\sim 2$ – $4$  km and an airspeed of  $\sim 100$ – $150$  m s $^{-1}$ , yielding along-track sampling by IWRAP of  $\sim 100$ – $150$  m. More details on IWRAP can be found in Fernandez et al. (2005).

The HIWRAP airborne Doppler radar was developed at the NASA Goddard Space Flight Center (GSFC) with the goal of studying hurricane genesis and intensification as well as other precipitating systems. One of the unique features of HIWRAP is its ability to fly on NASA's GH unmanned aircraft, which operates at  $\sim 18$ – $20$ -km altitude and can remain airborne for more than 24 h. HIWRAP is a dual-frequency (Ku and Ka bands), single-polarized (V for inner beam, H for outer beam), downward-pointing, and conically scanning (16 rpm) Doppler radar with two beams ( $\sim 30^\circ$  and  $40^\circ$ ) and 150-m range resolution. Figure 1b shows the scanning geometry of HIWRAP aboard the NASA GH, which has an airspeed of  $\sim 160$  m s $^{-1}$ , yielding  $\sim 600$  m along-track sampling. More details on HIWRAP can be found in Li et al. (2008).

Both radars complement each other well. For example, IWRAP has little to no attenuation at C band and very high-resolution capabilities, but the sensitivity of the C-band (and Ku band) signals are relatively low with quality measurements for moderate to intense precipitation only. In addition, IWRAP flies at low altitudes, which limits the vertical profiling capability as well as

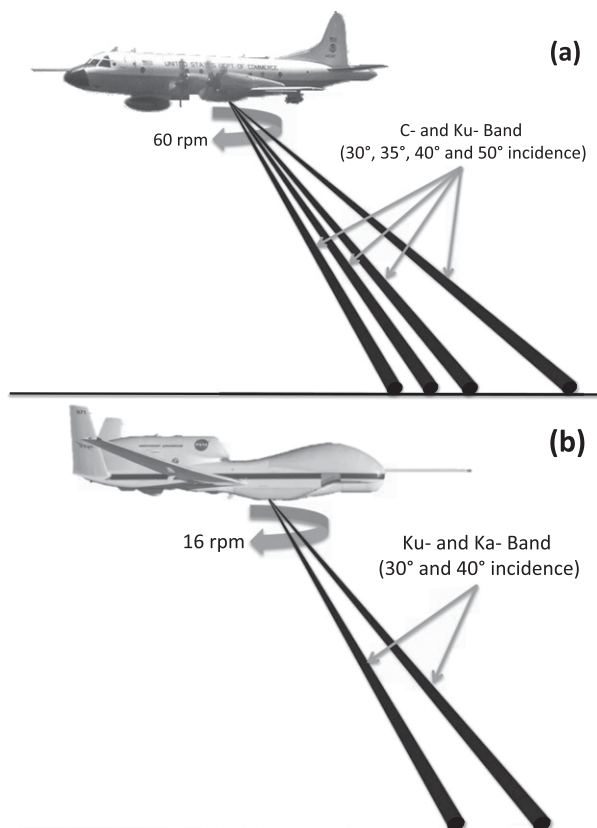


FIG. 1. Measurement geometry for (a) IWRAP aboard the NOAA WP-3D aircraft with typical flight altitudes of  $\sim 2$ – $4$  km and (b) HIWRAP aboard the NASA GH aircraft with typical flight altitudes of  $\sim 18$ – $20$  km.

the swath width (up to  $\sim 10$  km at the surface). The HIWRAP radar is able to fill some of the gaps left by IWRAP, although the very high-resolution and C-band measurements are unique to IWRAP. The HIWRAP is able to measure the full troposphere, has a wider swath ( $\sim 30$  km at the surface), and is able to detect light precipitation and some cloud at Ka band. Both radars are able to derive ocean surface vector winds through scatterometry retrieval techniques.

### b. Description of wind retrievals

Retrievals of the three Cartesian wind components over the entire viewing region or swath of IWRAP/HIWRAP can be performed using either a traditional least squares approach or through a variational procedure. In both methods, the radar swath is divided up into discrete cells with horizontal grid spacing typically larger than the along-track sampling and vertical grid spacing approximately equal to the range resolution. Radial velocity observations are assigned to each grid point by gathering data within an influence radius (in the

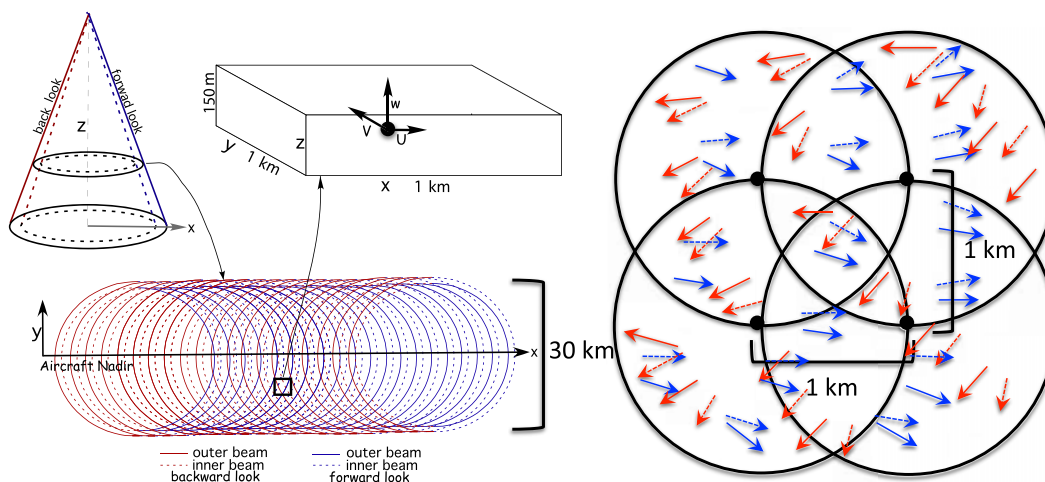


FIG. 2. Scan pattern and grid structure methodology for HIWRAP. The forward and backward portions of the scan are labeled in blue and red, respectively. The inner beam ( $30^\circ$ ) and outer beam ( $40^\circ$ ) are shown in dashed and solid lines, respectively. The influence radii shown are only 1 km for illustration but are larger for calculations. The arrows inside the influence radii represent the HIWRAP radial velocities with the color and line representations the same as that described above. See text for more details.

horizontal plane) from the grid point. The level of smoothness desired in the wind vector solution, with larger radii allowing smoother solutions by attenuating high frequencies, dictates the choice of influence radius. The influence radii are discussed in detail in the next section.

The radial velocity observations are corrected for velocity ambiguities and aircraft motion using the following procedure. For HIWRAP, dual pulse repetition frequency (PRF) sampling is employed with Nyquist intervals for the low and high PRF at Ku band (our focus in this paper) of  $19.6$  and  $24.5 \text{ m s}^{-1}$ , respectively. Combining these PRFs provides an extended Nyquist interval of  $\sim \pm 100 \text{ m s}^{-1}$  that is used to dealias [following Eqs. (7.9a) and (7.9b) in Doviak and Zrnić 1993] the single PRF velocity data, which have a lower uncertainty relative to the dual-PRF estimates (e.g., Doviak and Zrnić 1993, 171–175). After the dealiasing, the HIWRAP velocities are corrected for aircraft motion following Lee et al. (1994). For IWRAP, the C-band radial velocities (our focus in this paper) have a Nyquist interval of  $\sim \pm 225 \text{ m s}^{-1}$  and no dealiasing is required. The correction for aircraft motion is similar to that used for HIWRAP. Note that the IWRAP Ku-band velocities can be dealiased using the C-band velocities.

Figure 2 summarizes the grid structure methodology described above for HIWRAP with  $1 \text{ km} \times 1 \text{ km} \times 0.15 \text{ km}$  grid cells. In Fig. 2, the outline of the conical scan (inner beam at  $30^\circ$  and outer beam at  $40^\circ$ ) in track-relative coordinates is shown at the surface with the forward and backward portions of the scan labeled. The right side of Fig. 2 shows how radial velocity

observations are assigned to each grid point with oversampling providing smoothing. The influence radii capture azimuth diversity in the radial velocities afforded by the intersections of the forward and backward portions of the conical scan. This azimuth diversity and the steep incidence angles of the radar beams are used to recover the three Cartesian wind components at each grid point. Note that the grid structure methodology shown in Fig. 2 is the same for IWRAP, only the grid cells are typically  $0.20\text{--}0.25 \text{ km}$  in the horizontal and  $0.03 \text{ km}$  in the vertical.

Figure 3a illustrates the maximum azimuth diversity for the HIWRAP geometry and grid structure methodology outlined in Fig. 2 as a function of across-track distance and height. For this calculation, simulated data are used (see section 3) and the influence radii are specified as a function of height, with radii ranging from  $\sim 4 \text{ km}$  at the surface to  $\sim 1 \text{ km}$  at  $15\text{-km}$  height. These radii were chosen based on wind vector sensitivity tests examining solution accuracy and damping characteristics with simulated data. The influence radii are designed to become smaller with height because of the nature of the inverted cone radar scanning geometry (see the sketch of radar scans at two different levels in Fig. 2). More information on the influence radii can be found in the next section when the least squares approach is described. The azimuth diversity for each grid point is computed by finding the largest azimuth difference between pairs of observations within the influence radii. Large values of azimuth diversity close to  $90^\circ$  (optimal for horizontal winds) are found in two patches  $\sim 5\text{--}7 \text{ km}$  off nadir. Most of the swath has azimuth diversity near  $80^\circ$  with strong gradients that approach  $40^\circ$  at nadir,

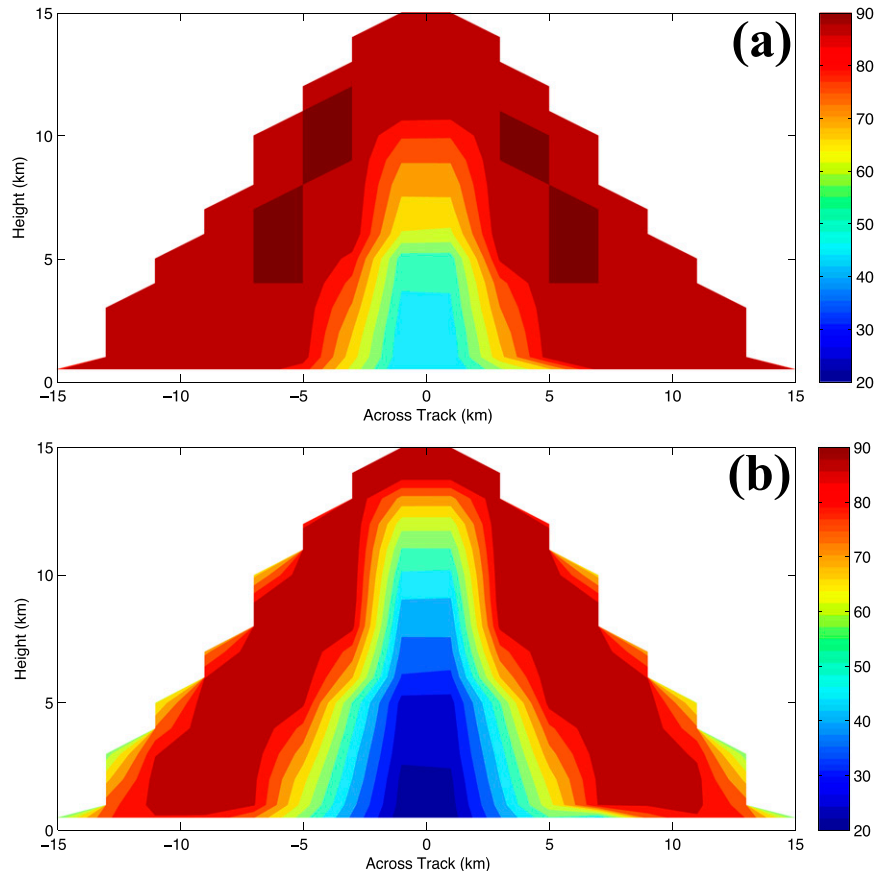


FIG. 3. Maximum azimuth diversity ( $^{\circ}$ ) for the HIWRAP geometry and grid structure methodology outlined as in Fig. 2, except the influence radii are (a)  $\sim 4$  km at the surface and  $\sim 1$  km at 15-km height and (b)  $\sim 1.8$  km at the surface and  $\sim 0.8$  km at 15-km height. See text for details.

where the diversity is smallest. Several Doppler radar studies have identified  $\sim 30^{\circ}$  of azimuth diversity as a lower bound for determining reasonably accurate horizontal wind components (e.g., Klimowski and Marwitz 1992). The large values of azimuth diversity shown in Fig. 3a are possible because of the large, overlapping influence radii that are used to gather radar observations at each analysis grid point. However, as described in the next section, the observations in the influence radii are weighted based on the distance from the analysis grid point, which will produce somewhat smaller levels of azimuth diversity than those shown in Fig. 3a. Smaller influence radii will produce more narrow zones of large azimuth diversity with values that go below  $\sim 30^{\circ}$  at nadir.

Figure 3b is the same as Fig. 3a, only the influence radii are  $\sim 1.8$  km at the surface and decrease to  $\sim 0.8$  km at 15-km height. The smaller influence radii decrease the azimuth diversity to a minimum of  $\sim 20^{\circ}$  at nadir with the region of largest diversity confined to

two thin bands between  $\pm 5$  and 10 km across track. In addition, the edges of the radar swath have reduced azimuth diversity, which results from the viewing geometry becoming collinear right along the swath edges (see Fig. 2). This edge effect does not appear in Fig. 3a because the influence radii are larger, which pulls in radial velocities from the swath interior that have larger azimuth diversity, resulting in larger maximum values. Despite this, the retrieved wind fields along the swath edges are still subject to the collinear nature of the viewing geometry due to the distance weighting in the solution procedure (see next section). Note that the results shown in Fig. 3 are nearly identical for IWRAP, only the radar is typically located between 2- and 4-km heights.

#### 1) THE LEAST SQUARES APPROACH

In the least squares approach, solutions for the wind components are found by solving a weighted least squares problem at each grid point using



$$J_o = \|\mathbf{W}(\mathbf{f} - \mathbf{E}\mathbf{g})\|^2. \quad (1)$$

In Eq. (1),  $J_o$  is termed the observation error cost function,  $\mathbf{f}$  is a column vector of  $m$  Doppler velocity observations (after being corrected for aircraft motions, velocity ambiguities, and hydrometeor fall speeds),  $\mathbf{g} = [u \ v \ w]^T$  is a column vector of the three unknown Cartesian wind components, and  $\mathbf{E}$  is a rotation matrix that maps the radar spherical coordinates to Cartesian space, described later. The double vertical bars represent the Euclidean norm. The  $\mathbf{W}$  in Eq. (1) is an  $m \times m$  diagonal matrix of Gaussian weights (also known as a Barnes weighting scheme) with diagonal elements given by

$$W_i = \exp \left[ - \left( \frac{r_o^i}{\gamma \delta} \right)^2 \right], \quad (2)$$

where  $r_o^i$  is the radius of the  $i$ th observation from the analysis grid point,  $\gamma$  is a shape parameter that determines the width of the weighting function, and  $\delta$  is the influence radius expressed as

$$\delta = s\beta \left( 1 - \frac{L_k}{H} \right) + s, \quad (3)$$

where  $s$  is the along-track sampling of the radar,  $\beta$  is a chosen smoothing factor,  $L_k$  is the  $k$ th vertical level of the analysis grid, and  $H$  is the average height of the radar.

The term  $\beta$  is a free parameter that determines the size of the influence radii. A larger value of  $\beta$  produces larger radii, which increases the number of points used to solve for the winds, including oversampling with neighboring grid points (see Fig. 2). These smoothing effects result in an increase of the signal-to-noise ratio and azimuth diversity, which will increase the accuracy of the wind vector solutions, provided the smoothing is not too large. However, larger values of  $\beta$  also decrease the effective resolution of the wind field analysis, where we define “effective resolution” as that radius where the weighting function in Eq. (2) reaches exponential decay

(falls off to  $e^{-1}$ ; e.g., Koch et al. 1983). The term  $\gamma$  has similar effects to  $\beta$ , determining the width of the filter response within the influence radius.

Wind vector solution sensitivity tests and spectral analysis (using simulated data described in section 3) with different values of  $\beta$  and  $\gamma$  indicated that a value of  $\beta \approx 6$  and  $\gamma = 0.75$  were reasonable (in terms of accuracy and damping characteristics) for this study. For a typical HIWRAP height of  $\sim 18$  km and along-track sampling of  $\sim 0.6$  km, values of the influence radii range from  $\sim 4$  km at the surface to  $\sim 1$  km at 15-km height. This results in effective resolutions of  $\sim 3$  km at the surface to just under 1 km at 15-km height.

The covariance matrix of the Doppler velocity observations is diagonal (each observation is independent of the others) and the variance of each measurement is directly proportional to the spectrum width, which is a function of several factors, including turbulence, shear, platform motion, and particle fall speeds (Doviak and Zrnić 1993). In this paper, we assume that the spectrum widths are constant, which results in constant Doppler velocity variances. As a result, we use observation weights [see Eq. (2)] based only on the distance from the analysis grid point. This is not without precedence, as Reasor et al. (2009) and López-Carrillo and Raymond (2011) employ a similar formulation for the observation weights. Calculations of the spectrum width and observation variances are being considered for future versions of the observation weight.

Finally, in Eq. (1)  $\mathbf{E}$  is an  $m \times 3$  matrix of coordinate rotations to map the radar spherical coordinates to Cartesian space:

$$\mathbf{E}_{m \times 3} = \begin{pmatrix} x_1 r_1^{-1} & y_1 r_1^{-1} & z_1 r_1^{-1} \\ \vdots & \vdots & \vdots \\ x_m r_m^{-1} & y_m r_m^{-1} & z_m r_m^{-1} \end{pmatrix}, \quad (4)$$

where  $r_m$  is the range for the  $m$ th observation and the Earth-relative coordinates centered on the radar are given by (index subscript  $m$  dropped here for convenience)

$$\begin{pmatrix} x \\ y \\ z \end{pmatrix} = r \begin{bmatrix} \cos H(a) + \sin H \sin \tau(b) + \sin H(c) \\ -\sin H(a) + \cos H \sin \tau(b) + \cos H(c) \\ \sin \tau(\sin P \cos \theta - \cos P \sin R \sin \theta) - \cos P \cos R \cos \tau \end{bmatrix}, \quad (5)$$

where

$$\begin{pmatrix} a \\ b \\ c \end{pmatrix} = \begin{pmatrix} \cos R \sin \theta \sin \tau - \sin R \cos \tau \\ \cos P \cos \theta + \sin P \sin R \sin \theta \\ \sin P \cos R \cos \tau \end{pmatrix} \quad (6)$$

and  $P$ ,  $R$ ,  $\theta$ ,  $H$  and  $\tau$  are the pitch, roll, azimuth, heading, and tilt angles, respectively. Equation (5) is derived for the IWRAP/HIWRAP geometry following Lee et al. (1994), and all angle conventions and coordinate systems follow this paper as well.

The unknown wind components  $\mathbf{g}$  are found by solving the normal equations, which are formed by finding where the partial derivatives of  $J_o$  with respect to the unknown parameters (wind components) are equal to zero, yielding

$$\mathbf{g} = (\mathbf{E}^T \mathbf{W} \mathbf{E})^{-1} \mathbf{E}^T \mathbf{W} \mathbf{f}. \quad (7)$$

Equation (7) is solved directly using a Cholesky decomposition/Gaussian elimination algorithm. Ray et al. (1978) and earlier papers such as Heymsfield (1976) were among the first studies to apply the basic formulation of the least squares approach for retrieving the Cartesian wind components from ground-based Doppler radar.

The main advantages of the least squares approach relative to the variational method (described next) are the computational efficiency [the setup and solution of Eq. (7) are done when assigning observations to each grid point, which takes a trivial amount of computer time] and the ability to analyze the theoretical uncertainty in the wind components through an error propagation analysis.

The general formula for error propagation is

$$\delta q^2 = \sum_i \left( \frac{\partial q}{\partial x_i} \delta x_i \right)^2, \quad (8)$$

where  $\delta q$  represents the Gaussian uncertainty in  $q$  (a function of  $x_i$ ), and each  $x_i$  denotes a variable with associated uncertainty  $\delta x_i$  that contributes to the calculation of  $\delta q$ . Applying Eq. (8) to Eq. (7) we obtain

$$\delta \mathbf{g}^2 = k k^T M, \quad (9)$$

where  $k = (\mathbf{E}^T \mathbf{W} \mathbf{E})^{-1} \mathbf{E}^T \mathbf{W}$  and  $M = J_o/d$  is the mean-square error of the weighted least squares fit with  $d = m - 3$  representing the degrees of freedom: the number of observations assigned to each grid point minus the number of estimated parameters. In Eq. (9), the mean-square error is used to model the uncertainties in the Doppler velocity observations ( $\delta \mathbf{f}$ ) because this quantity is more relevant to the theoretical treatment of the least squares parameter errors considered here (Strang 1986). By applying the matrix product identity on  $k^T$  in Eq. (9), we arrive at the final equation for the variance in the least-squares-estimated Cartesian wind components considered in this paper:

$$\delta \mathbf{g}^2 = (\mathbf{E}^T \mathbf{W} \mathbf{E})^{-1} \mathbf{E}^T \mathbf{W} \mathbf{W}^T \mathbf{E} (\mathbf{E}^T \mathbf{W} \mathbf{E})^{-1} M. \quad (10)$$

A desirable feature of this error propagation analysis is the ability to analyze the errors in the retrieved wind

components when no supporting data are available (the usual case). An examination of the usefulness of these fields will be presented in section 3a.

## 2) THE VARIATIONAL APPROACH

The variational approach extends the least squares method by adding constraints to the basic observation error cost function shown in Eq. (1). Typically, these constraints include the anelastic mass continuity equation, which has been shown to improve retrievals of the vertical velocity for ground-based radars (Gao et al. 1999), and a spatial filter to control noise (Sasaki 1970; Yang and Xu 1996). The real value of the variational approach is the ability to evaluate and satisfy dynamic constraints on the wind field simultaneously with the observation term, which avoids errors (e.g., boundary conditions and error accumulation) associated with the explicit integration of some constraints, such as the mass continuity equation (see Potvin et al. 2012 for more discussion).

For ground-based radars where much of the vertical velocity is poorly sampled, the mass continuity constraint will improve the accuracy of retrieved vertical velocities more than those computed from IWRAP/HIWRAP, where the vertical velocity is sampled relatively well. The incidence angles of IWRAP/HIWRAP are steep and  $\sim 77\%$ – $87\%$  (for incidence angles between  $30^\circ$  and  $40^\circ$ ) of the true vertical velocity is measured. For the retrieval of the horizontal velocities, the opposite is true: the mass continuity constraint will tend to have a smaller impact for ground-based radars (horizontal velocities are sampled well) and a larger impact for IWRAP/HIWRAP (horizontal velocities are not sampled as well as ground-based radars). Accurate retrievals of the horizontal velocities are still possible with IWRAP/HIWRAP because the horizontal velocities have a much larger signal than the vertical velocities, especially at the lower levels in a hurricane.

The cost function for our variational approach follows the tradition described in the papers above and takes the continuous form

$$J = J_o + \alpha_M \left\| \left( \frac{\partial u}{\partial x} + \frac{\partial v}{\partial y} + \frac{1}{\rho} \frac{\partial \rho w}{\partial z} \right) \right\|^2 + \alpha_S (\|\nabla^2 u\|^2 + \|\nabla^2 v\|^2 + \|\nabla^2 w\|^2), \quad (11)$$

where  $\alpha_M$  and  $\alpha_S$  are the weights for the anelastic mass continuity equation and the Laplacian spatial filter, respectively, and  $\rho = \rho(z)$  is an environmental density profile. In addition to the mass continuity and filtering constraints, the impermeability condition is imposed at the ground ( $w = 0$  at  $L_I = 0$ ). The procedure for finding



$\mathbf{g}$  in the variational approach initially proceeds in the same fashion as in the least squares method: take the partial derivatives of  $J$  with respect to  $\mathbf{g}$  and set these equations equal to zero. However, instead of solving for  $\mathbf{g}$  using linear algebra and a Gaussian elimination algorithm,  $\mathbf{g}$  is found using an iterative, nonlinear conjugate gradient algorithm [the conjugate gradient minimization (CONMIN) software package was used; Shanno 1978; Shanno and Phua 1980]. A modern recoding of CONMIN in MATLAB was performed and the function [Eq. (11)] and gradient [not shown, but similar to Gao et al. (1999)] evaluations are input into the algorithm for each iterative search for the minimum. The function and gradient evaluations are discretized to second-order accuracy.

The values of the weights are determined by trial and error using a numerical simulation of a hurricane (described in the next section) as truth. Values of  $2\Delta x^2$  for  $\alpha_M$  and  $0-O(\Delta x^4)$  for  $\alpha_S$  are deemed reasonable, where  $\Delta x^2$  and  $\Delta x^4$  are the square and fourth power of the horizontal grid spacing, respectively [a scaling to keep the units consistent with  $J_o$  in Eq. (11)]. Small perturbations to the chosen weights for the dynamic constraints did not have a significant effect on the solutions, which was also found by Shapiro et al. (2009). A value of unity is used for  $J_o$ .

Smoothing is already contained in the oversampling of observations used to solve the observation error term in Eq. (11), so values of  $\alpha_S = 0$  were sufficient for the simulated data with  $\pm 1\text{--}2\text{ m s}^{-1}$  random noise (discussed in the next section). For measured radar observations with significant noise, the Laplacian filter is more important ( $\alpha_S \sim \Delta x^4$ ) to enable convergence of the minimization algorithm and for obtaining reasonably smooth solutions. In the next section, a discussion of the error characteristics of both the least squares and variational solutions for simulated data will be presented. The focus of the variational discussion will be on the improvements to the least squares solutions.

### 3. Error characteristics

A numerical simulation of Hurricane Bonnie (1998) at 2 km horizontal and  $\sim 0.65$  km vertical (27 levels) resolutions described in Braun et al. (2006) was used to study the error characteristics of the wind retrieval algorithms. For this simulator we have focused on the HIWRAP radar, but because the scanning geometry and retrieval methods are the same, the errors for IWRAP will be similar. The numerical simulation revealed a realistic, environmental wind-shear-induced, wavenumber 1 asymmetry in the storm core with embedded deep convective towers and mesovortices [see Braun et al.

(2006) for displays of the storm structure]. These structures are common in nature, and they provide a good test case for evaluating the performance of the wind retrieval algorithms.

The simulated storm is repositioned in the center of the model domain (2-km-resolution portion covers  $\sim 450\text{ km}^2$ ) to allow for the use of a storm-centered retrieval grid. The GH aircraft is initialized in a portion of the domain, and characteristic HIWRAP scan parameters are set as follows: two beams ( $30^\circ$  and  $40^\circ$  incidence),  $2^\circ$  azimuthal sampling, 0.60-km along-track sampling (based on an airspeed of  $160\text{ m s}^{-1}$ ), and 0.15-km gate spacing. The GH attitude parameters are taken from real data during flights over TCs during GRIP. The mean and standard deviation of the aircraft attitude parameters are altitude ( $18.5 \pm 0.1\text{ km}$ ), pitch ( $2.5^\circ \pm 0.5^\circ$ ), and roll ( $0^\circ \pm 0.5^\circ$ ). In the implementation of the simulated flights, random perturbations with a uniform distribution and upper limits dictated by the standard deviations are added to the mean values of the attitude parameters.

The Bonnie simulated wind fields ( $u$ ,  $v$ , and  $w$ ) are interpolated to the radar points and the radial velocities are calculated using

$$V = (ux + vy + wz)r^{-1}, \quad (12)$$

where  $x$ ,  $y$ , and  $z$  are given in Eq. (5). The hydrometeor fall speed is set to zero when computing the radial velocities. Random errors of  $\pm 1\text{--}2\text{ m s}^{-1}$  with a uniform distribution were added to the radial velocities to simulate the typical uncertainties of measured Doppler velocities from IWRAP and HIWRAP with signal-to-noise ratios of  $\sim 10\text{ dB}$  or larger (typical of the hurricane eyewall; Fernandez et al. 2005). Larger errors are considered to examine the robustness of the retrieval statistics and will be noted where appropriate. The two sources of error examined with the simulated wind field are those from the airborne radar geometry (including aircraft attitude) and noise in the Doppler velocities. Note that measured Doppler velocities encompass a number of systematic errors (e.g., aliasing, antenna pointing errors, beam filling issues) that are not addressed with the simulator. Hydrometeor fall speed uncertainties are not considered in the simulator either, but comparisons of measured retrievals to flight-level data in the rain region of a hurricane are described in section 4.

A retrieval grid centered on the storm center that covers  $250\text{ km}^2$  in the horizontal with 2-km grid spacing (to match the numerical simulation) and 15 km in the vertical with 1-km grid spacing (an extra level at 0.5 km was added to sample winds in the boundary layer and a level at 0 km is used for the impermeability condition)

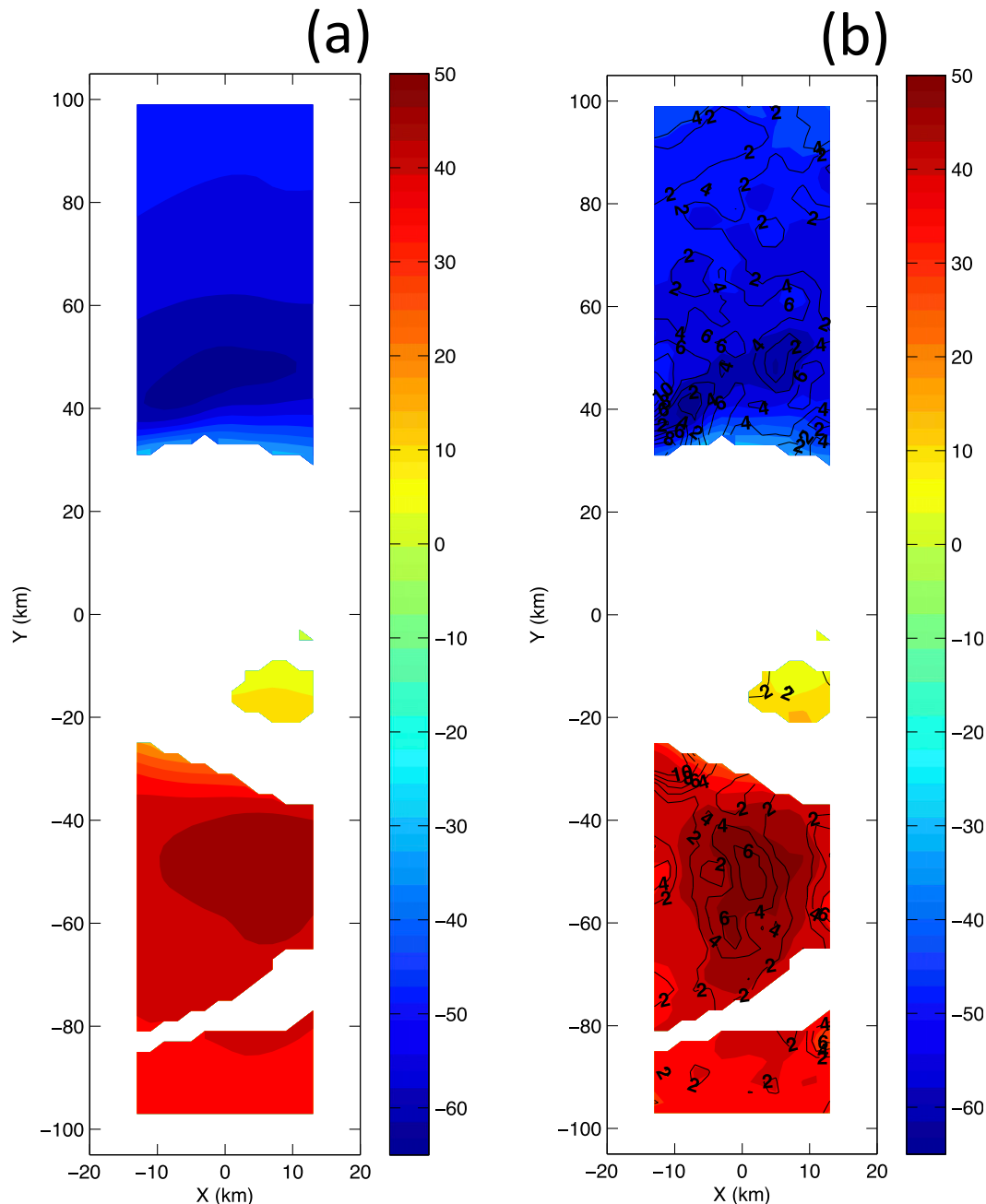


FIG. 4. Simulated HIWRAP zonal velocity at 1-km height for a northerly GH track across the eyewall of Hurricane Bonnie (1998) at 1200 UTC 23 Aug 1998. The shading shows (a) the model truth field and (b) the retrieval field with the black contours revealing the RMSEs with a contour interval of  $2 \text{ m s}^{-1}$  from 2 to  $10 \text{ m s}^{-1}$ . Fields are only shown where the simulated reflectivity is greater than 0 dBZ.

was created. The three Cartesian velocity components are then computed on this grid (except at 0 km) using the least squares and variational retrieval methods.

Three aircraft flight patterns were considered for the simulator: 1) a straight-line segment  $\sim 200 \text{ km}$  in length in a weaker portion of the model domain with maximum winds of  $\sim 30 \text{ m s}^{-1}$ , 2) a straight-line segment  $\sim 200 \text{ km}$

in length across the eyewall of Bonnie with maximum winds of  $\sim 60 \text{ m s}^{-1}$ , and 3) a 1.8-h rotated figure-four pattern centered on the storm center with  $\sim 100\text{-km}$  radial legs. The rotated figure four (see Fig. 15 for an example) is the most common TC flight pattern for the IWRAP and HIWRAP radars. The qualitative structure of the root-mean-square errors (RMSEs) for each wind

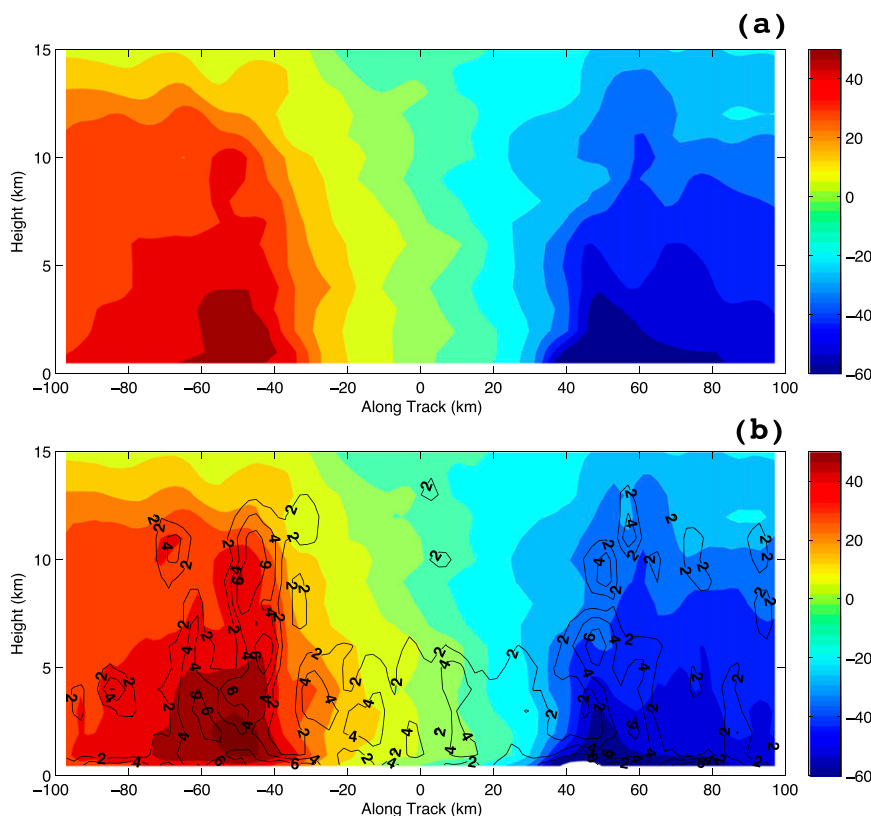


FIG. 5. Comparison of (a) simulated truth and (b) retrieved zonal velocity structure at nadir for the eyewall flight segment described in the text. The black contours in (b) show the RMSEs at 2, 4, and 6  $\text{m s}^{-1}$ . Note that no reflectivity mask is applied to these fields and that the vertical axis is exaggerated to show detail.

component was similar for the weak and eyewall flight segments, so we focus here on the eyewall segment because the sharp gradients of the eyewall are more challenging for the retrieval algorithms.

#### a. Eyewall flight segment

##### 1) LEAST SQUARES SOLUTION

Figure 4a shows the zonal (across track) velocity field for the simulated truth field at 1-km height for a northerly GH heading across the simulated eyewall of Bonnie at 1200 UTC 23 August 1998 with maximum zonal wind speeds of  $\sim 60 \text{ m s}^{-1}$ . The retrieved zonal wind speeds along with the RMSEs at 1-km height are shown in Fig. 4b. The RMSEs are typically largest ( $>6 \text{ m s}^{-1}$ ) at the junction between the inner edge of the eyewall and the edge of the swath. This structure is due to the sharp gradients of the eyewall interface, which are difficult to capture, and the poor azimuth diversity that occurs right along the edges of the radar scan (see discussion of Fig. 3 in section 2b). The least squares solution for the wind field incorporates all observations in the influence radius with the largest weight given to those observations closest

to the analysis grid point. This leads to a greater chance for errors and potentially unstable solutions along the swath edges. Away from the edges and the inner edge of the eyewall, the RMSEs in Fig. 4b are mostly  $2\text{--}4 \text{ m s}^{-1}$  even in the core of the eyewall, where the wind speeds are large. Note that across-track winds can be retrieved at nadir because the influence radii at nadir grid points allow for enough azimuth diversity (see Fig. 3) to compute the horizontal wind vector.

Figures 5a and 5b show vertical cross sections at nadir of the across-track velocity from the simulated truth and retrievals, respectively. The main structural features of the simulated truth field, such as the radius of maximum winds, eyewall slope, and decay of winds with height, are captured well by the retrievals. The majority of the errors are  $\sim 2\text{--}4 \text{ m s}^{-1}$  in the core of the eyewall (approximately  $\pm 40\text{--}60 \text{ km}$  along track) with lower values outside of this region. The largest errors of  $\sim 6 \text{ m s}^{-1}$  occur mostly in the boundary layer and on the southern side of the storm (around  $-50 \text{ km}$  along track) in a few patches extending from low levels up to  $\sim 10\text{-km}$  height.

Figure 6a shows the RMSEs for the across-track velocity averaged along track for the eyewall flight segment.

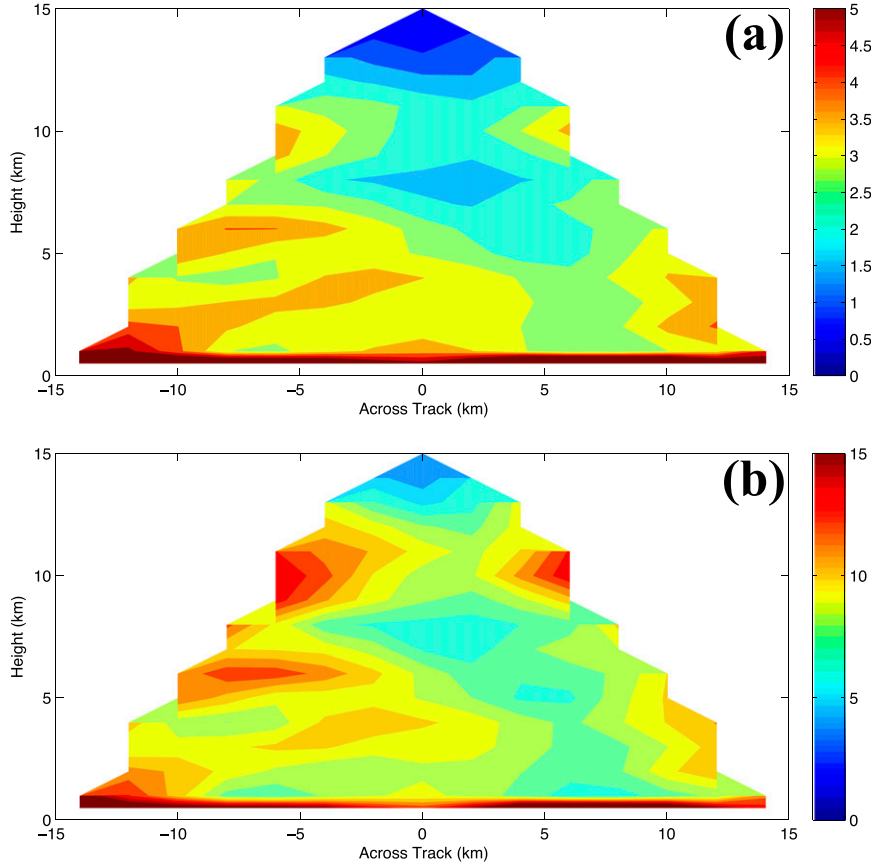


FIG. 6. Simulated HIWRAP zonal velocity retrieval errors for the same flight track as that shown in Fig. 4. In these figures, the averages are taken in the along-track direction. The shading shows the (a) RMSEs and (b) RELs.

This figure (and subsequent plots for the other wind components) is intended to summarize the error structure of the downward-pointing, conically scanning radar. The largest RMSEs of  $5 \text{ m s}^{-1}$  or greater occur in the boundary layer, where the wind speeds, variance, and gradients in the eyewall are large. Above  $\sim 1\text{-km}$  height, the RMSEs are largely  $2\text{--}3 \text{ m s}^{-1}$  with the lowest values of  $\sim 1 \text{ m s}^{-1}$  found above  $10\text{-km}$  height. There are also indications of larger errors at the swath edges in Fig. 6a, consistent with Fig. 4 and associated discussion. The systematic error of the across-track velocity component for the eyewall flight segment is  $0.53 \text{ m s}^{-1}$ , where a positive value indicates the retrievals were larger than the model truth.

A more revealing error diagnostic for each velocity component is the relative RMSE (REL) expressed as

$$\text{REL} = \sqrt{\frac{\sum_{i=1}^n (X_i^T - X_i^R)^2}{\sum_{i=1}^n (X_i^T)^2}} \times 100, \quad (13)$$

where  $X_i^T$  is the model truth velocity component for each grid point  $i$ ,  $X_i^R$  is the retrieved velocity component, and  $n$  is the number of grid points. Figure 6b shows the RELs for the eyewall flight segment with the summations in Eq. (13) taken over the along-track grid points. The RELs in Fig. 6b are able to put the RMSEs in Fig. 6a into perspective, which is useful for understanding and generalizing the results. Above  $\sim 1\text{-km}$  height, the REL values are  $\sim 10\%\text{--}12\%$  on many of the swath edges and  $\sim 5\%\text{--}8\%$  everywhere else in the swath with the lowest values of  $\sim 5\%$  found above  $10\text{-km}$  height, consistent with Fig. 6a. The errors are lowest at upper levels because the azimuth diversity is maximized there, since all the radar-viewing angles collapse to one or two grid points (see Fig. 3).

Figure 7a shows the meridional (along track) velocity for the same flight track as in Fig. 4 at  $1\text{-km}$  height. The maximum meridional wind speed in this section of Bonnie's eyewall is  $\sim 20 \text{ m s}^{-1}$ . Figure 7b reveals that the along-track winds have very small RMSEs with the largest values of  $0.5\text{--}1.0 \text{ m s}^{-1}$  on the swath edges and values of  $0.25 \text{ m s}^{-1}$  or lower in the interior of the swath.

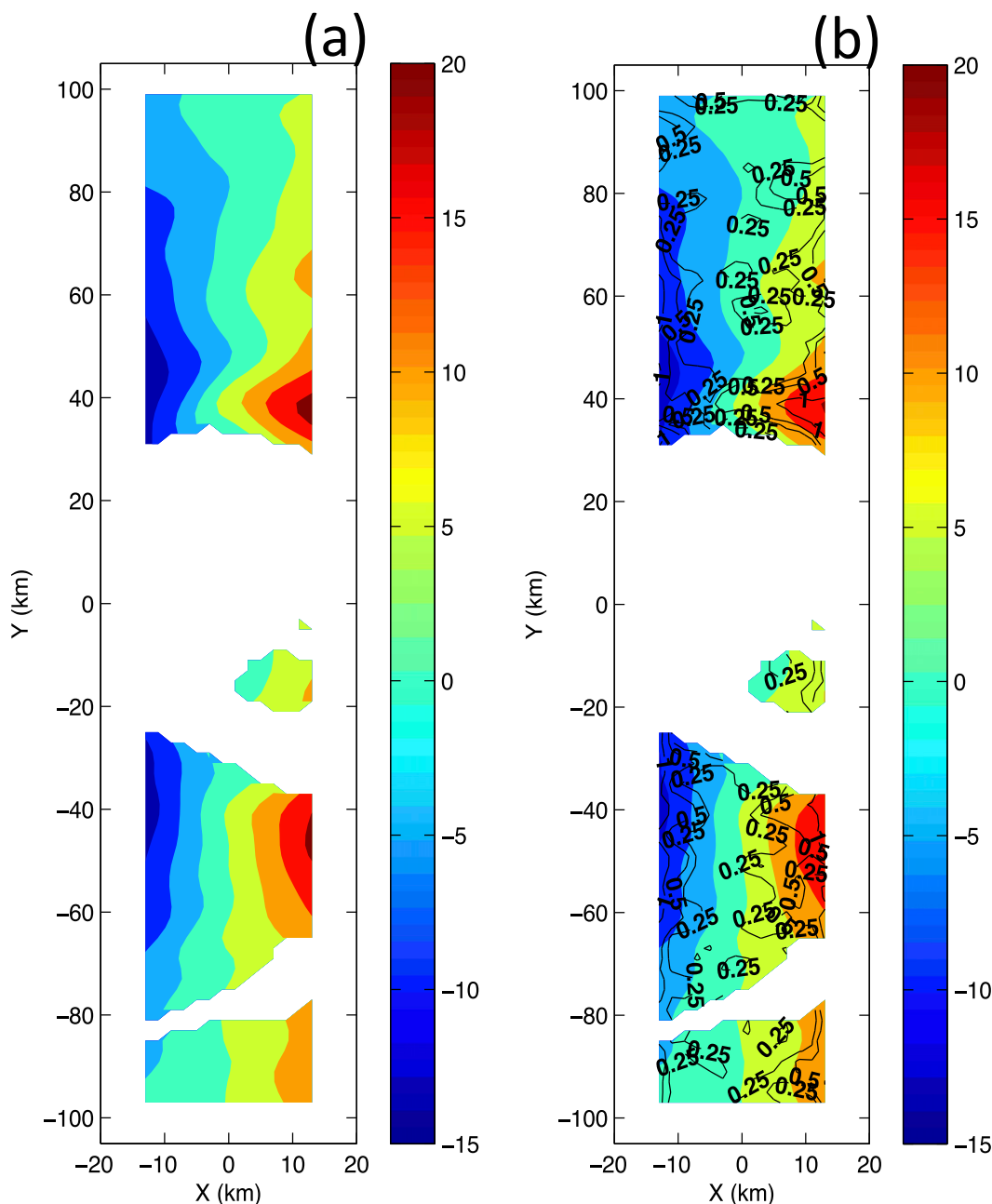


FIG. 7. As in Fig. 4, except for the meridional velocity with black error contours in (b) from  $0.25\text{--}1.0\text{ m s}^{-1}$  with a  $0.25\text{ m s}^{-1}$  interval.

This across-track structure for the along-track velocity can be understood by referring back to the COPLAN wind retrieval method described in the introduction. At nadir, the radar beams sample little across-track velocity and the along-track velocity can, in theory, be solved for exactly [Tian et al. (2011) discuss the COPLAN method applied to HIWRAP]. As the radar beams scan away from nadir, more across-track velocity is sampled and the along-track wind errors increase. The error structure

is similar at other levels and is not shown. Instead, to illustrate the vertical structure of the along-track winds, a vertical cross-section comparison is shown at nadir.

Figures 8a and 8b show the simulated truth and retrieved along-track winds at nadir, respectively. There is almost an exact match between the simulated truth and the retrieval fields with the only discernable errors, which are very small (largely  $0.25\text{ m s}^{-1}$  or less), occurring at or below 5-km height, especially on the southern

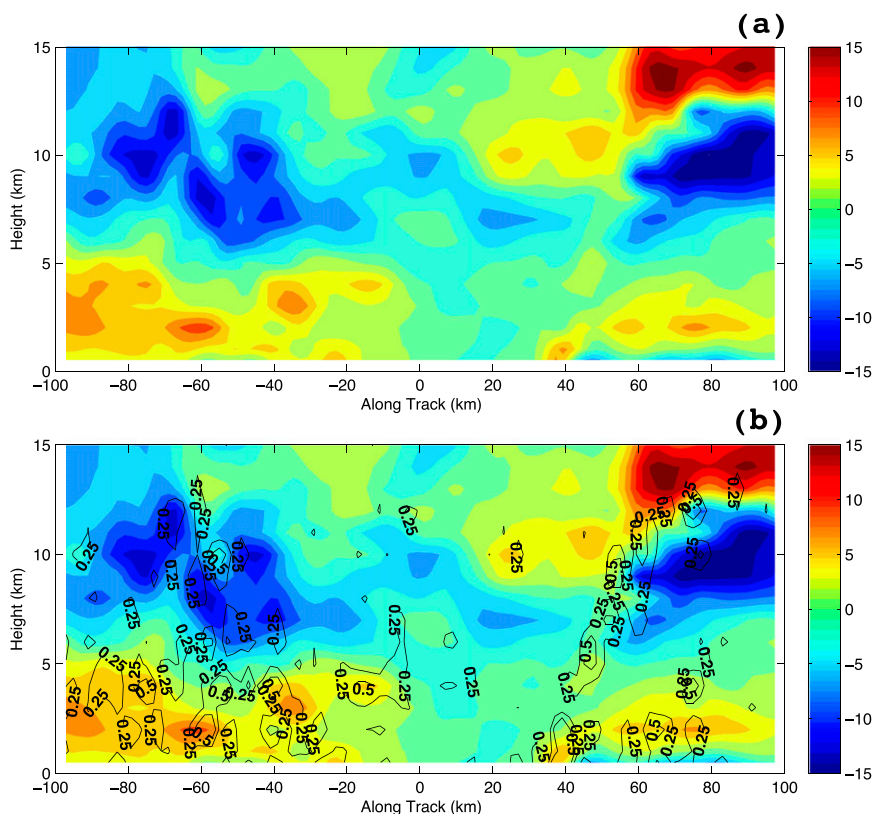


FIG. 8. As in Fig. 5, but for the meridional velocity. The black contours in (b) show the RMSEs at 0.25 and 0.50  $\text{m s}^{-1}$ .

side of the storm. There is also a region of 0.25  $\text{m s}^{-1}$  errors right along the edge of the eyewall sloping outward with height on both sides of the storm between  $\sim 40$  and 80 km along track.

Figure 9 shows the along-track averaged errors for the along-track velocity. The RMSEs in Fig. 9a reveal clear across-track dependence at all levels with the lowest errors at nadir, which was also seen in Figs. 7b and 8b. The largest errors are only  $\sim 1 \text{ m s}^{-1}$  at the swath edges below  $\sim 5$ -km height with the majority of the swath having RMSEs of  $\sim 0.25 \text{ m s}^{-1}$ . The RELs in Fig. 9b show large pockets with errors of only  $\sim 2\%$ . Even though the RMSEs are only  $1 \text{ m s}^{-1}$  at the swath edges, the RELs put this into perspective by revealing some larger values of  $\sim 15\%$  or greater in some spots. Overall, however, the RELs are still quite low with the majority of the swath having values less than 10%. The systematic error of the along-track velocity component for the eyewall flight segment is nearly zero.

Moving on to vertical velocity, Fig. 10 shows horizontal cross sections of vertical velocity at 8-km height. In the southern eyewall section of the simulated truth (Fig. 10a), a pronounced updraft/downdraft couplet with values of  $\sim 4 \text{ m s}^{-1}$  is visible. The corresponding retrieval

vertical velocities in Fig. 10b capture this structure fairly well over most of the swath (especially at nadir), but larger errors of  $0.5$ – $1.0 \text{ m s}^{-1}$  distort the retrieved vertical velocities toward the swath edges. In the northern section of the eyewall, larger errors at the swath edges are also apparent with the smallest errors of less than  $0.5 \text{ m s}^{-1}$  centered on the middle part of the swath.

Figure 11 shows the vertical structure of the vertical velocities at nadir from the simulated truth and the retrievals. The small errors at nadir shown in Fig. 10 are made very clear with the structural comparison in Fig. 11. There is a very close match between the simulated truth and the retrieval fields with the only discernable errors, which are small ( $0.25 \text{ m s}^{-1}$ ), occurring at the locations of the maximum updrafts as well as in the boundary layer. Off-nadir vertical cross-section comparisons of the vertical velocity (not shown) were also analyzed, and the core updraft/downdraft features are well resolved out to approximately  $\pm 5$  km from nadir with some larger errors present. Beyond  $\pm 5$ – $6$  km across track, errors in the vertical velocity structure become larger, as shown in Fig. 10.

Figure 12 shows the along-track averaged errors for the vertical velocity. The RMSEs in Fig. 12a have



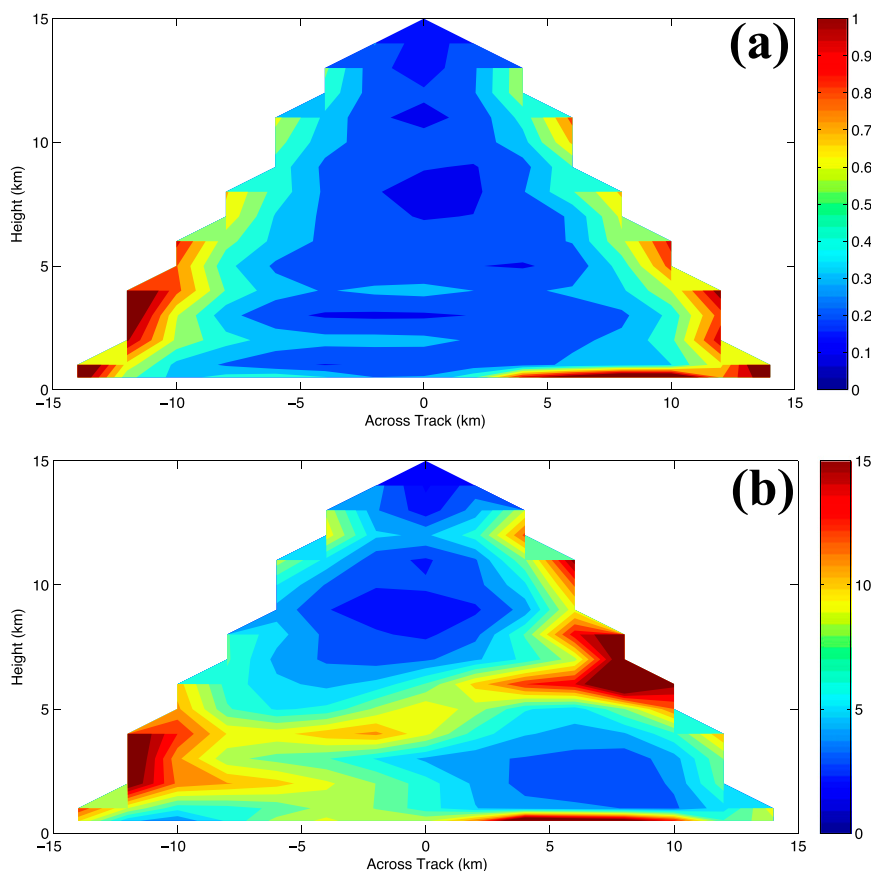


FIG. 9. As in Fig. 6, but for the meridional velocity.

strong across-track dependence with the lowest errors ( $\sim 0.25 \text{ m s}^{-1}$ ) at nadir and the largest errors ( $\sim 3\text{--}5 \text{ m s}^{-1}$ ) at the swath edges. This across-track structure is due to the same reasoning as that described for the along-track velocity above. That is, the solutions for the vertical velocity field described in this paper are approximations to the COPLAN method, which yields an exact expression for the vertical velocity at nadir. As the radar beams scan away from nadir, more across-track velocity is sampled and the vertical velocity errors increase. The RELs in Fig. 12b are very useful for placing the vertical velocity RMSEs in perspective. At nadir the REL values are  $\sim 25\%$ , which is excellent, and increase to several hundred percent at the swath edges below  $\sim 5\text{-km}$  height. Above  $\sim 5\text{-km}$  height, the RELs are lower with the 100%–150% contour extending out to the edges of the swath. The lower RELs above  $\sim 5\text{-km}$  height reflect the larger vertical velocities and smaller horizontal velocities at these levels. The systematic error of the vertical velocity component for the eyewall flight segment is  $-0.17 \text{ m s}^{-1}$ , where a negative value indicates the retrievals were smaller than the model truth.

The simulated errors presented in this section are a useful guide to the expected errors in the retrieved Cartesian wind components when using measured data. However, measured Doppler velocities can encompass more complicated errors (e.g., noise structure, missing data) and varying environmental flow scenarios that limit the use of simulated errors. The theoretical error propagation analysis derived in section 2b for the least squares approach is intended to provide error guidance when using measured Doppler velocity data and will be analyzed in section 4. Below, we briefly describe the correlation between the simulated and theoretical errors as an initial assessment of their value.

Figure 13 shows the standard deviations of the Cartesian wind components using the error propagation analysis. Figures 13a, 13b, and 13c show the across-track, along-track, and vertical standard deviations, respectively, for the same levels and flight track as in Figs. 4b, 7b, and 10b. The standard deviations are computed by taking the square root of the diagonal elements of  $\delta \mathbf{g}^2$  in Eq. (10). The spatial structure of the theoretical errors is highly correlated with the simulated errors, including regions of maximum/minimum

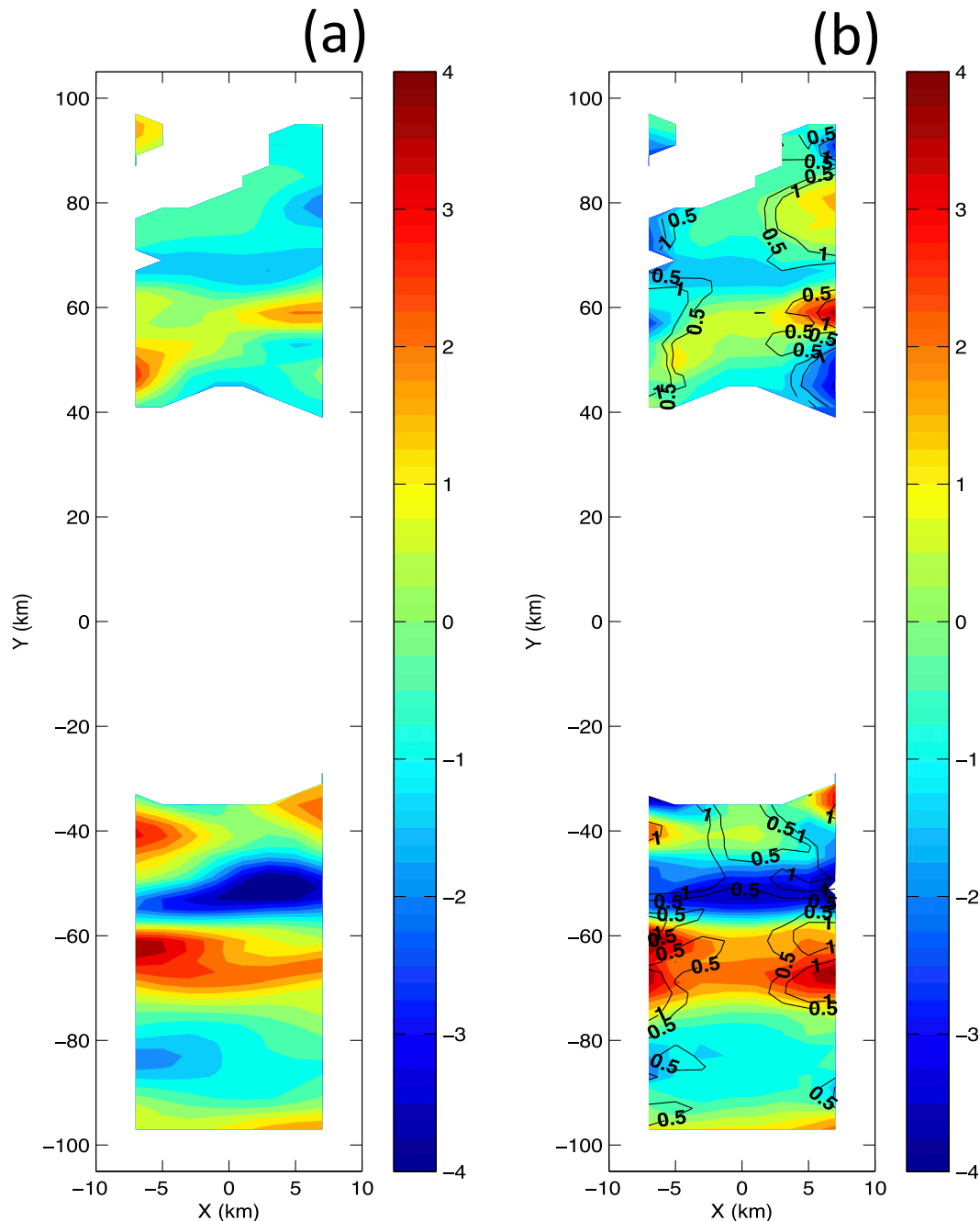


FIG. 10. As in Fig. 4, except for the vertical velocity at 8-km height with the black error contours in (b) drawn at  $0.5$  and  $1.0 \text{ m s}^{-1}$ .

values and the strong across-track dependence of the errors for the along-track and vertical components (cf. Figs. 4b, 7b, and 10b with Figs. 13a, 13b, and 13c, respectively). The magnitudes of the theoretical errors are typically lower than those for the corresponding simulated errors, especially for the across-track velocity. This is probably because the simulated errors are

more connected to the actual structure of the flow field, whereas the theoretical errors attempt to predict these errors by accounting for the quality of the least squares fit and the scanning geometry, including the weighting function. We believe the theoretical errors are still quite useful and can be regarded as a somewhat lower estimate of the simulated errors.

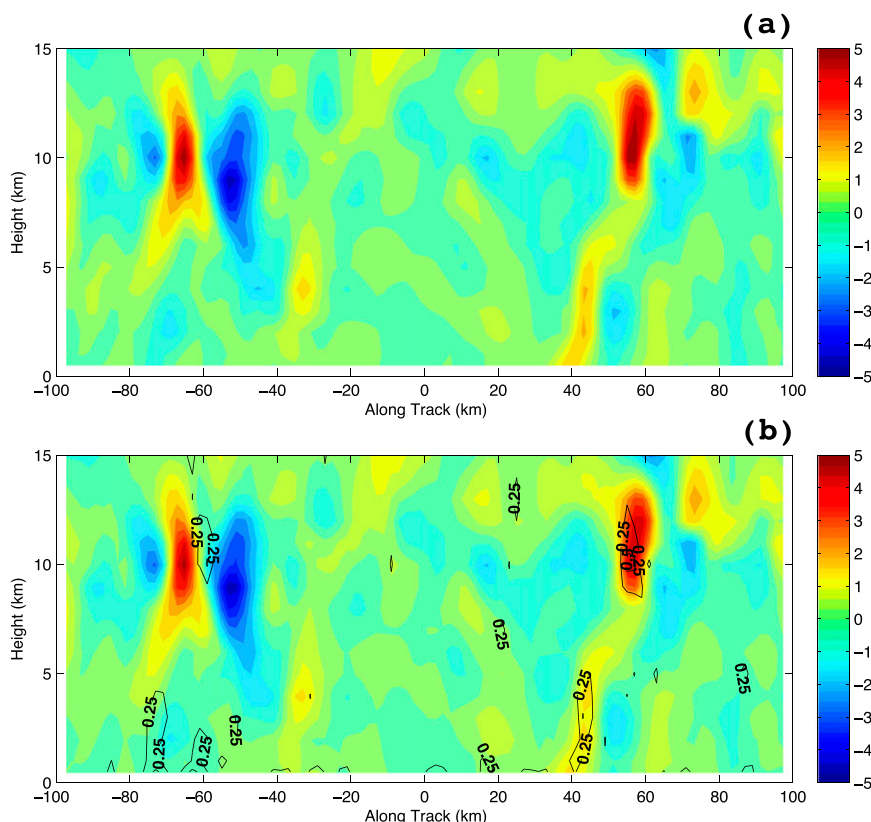


FIG. 11. As in Fig. 5, but for the vertical velocity. The black contours in (b) show the RMSEs at  $0.25 \text{ m s}^{-1}$ .

## 2) VARIATIONAL SOLUTION

In the variational method, adding the anelastic mass continuity constraint with the impermeability condition reduced the volume-averaged error, relative to the least squares approach, in the across-track and vertical velocity by  $\sim 0.80$  and  $\sim 0.50 \text{ m s}^{-1}$ , respectively. The along-track winds did not change much with the addition of the mass continuity constraint because the errors using the least squares method are already very low with little room for improvement. The one exception is a small area in the boundary layer at 0.5-km height and between 5 and 10 km across track (see Fig. 9a) where error reductions of up to  $\sim 0.50 \text{ m s}^{-1}$  were found.

To show the structure of the error reductions for the across-track and vertical velocities using the variational method, the RMSEs are averaged along track, which produces a figure similar to those shown in Figs. 6a and 12a. The RMSEs from the least squares solution are then subtracted from the variational ones to highlight regions where the errors are changing.

Figure 14a shows the differences between the variational and least squares RMSEs for the across-track

velocity. Negative values show where the variational solutions produced lower errors than the least squares method. The error differences in Fig. 14a (see Fig. 6a for the least squares errors) have strong across-track structure with the variational solutions reducing the across-track velocity errors the least at nadir ( $\sim 0.25 \text{ m s}^{-1}$ ) and the most at the swath edges, especially in the boundary layer (more than  $3 \text{ m s}^{-1}$ ). The largest reductions in errors of more than  $5 \text{ m s}^{-1}$  occur at the lowest analysis levels, where the mass continuity equation coupled with the impermeability condition are active. The impermeability condition proved to be an important component for reducing the errors, since without it only small reductions and some increases in errors occurred.

Figure 14b shows the error differences for the vertical velocity (see Fig. 12a for the least squares errors). The structure of this figure is very similar to the across-track figure, but the magnitudes of the error reductions are consistently lower everywhere ( $\sim 0.10 \text{ m s}^{-1}$  at nadir to more than  $2 \text{ m s}^{-1}$  at the swath edges in the boundary layer). The magnitudes are lower because the vertical velocity is sampled relatively well by IWRAP/HIWRAP (see discussion of the variational procedure in section

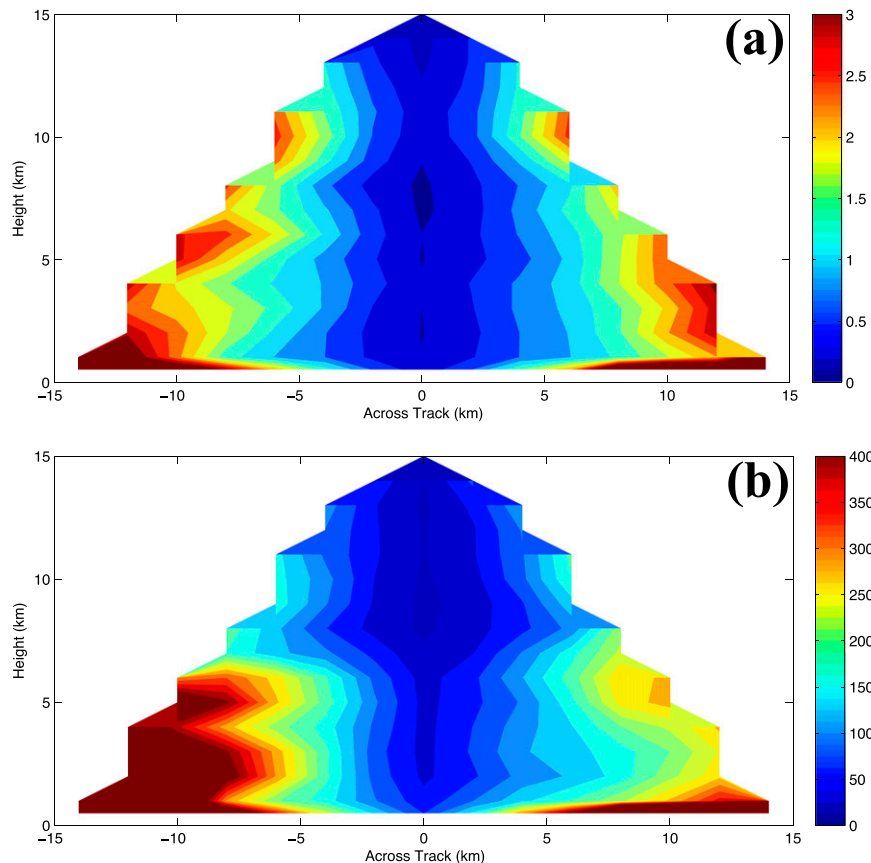


FIG. 12. As in Fig. 6, but for the vertical velocity.

2b). The large reductions in errors at lower levels shown in Fig. 14 are consistent with Potvin et al. (2012), where statistically significant improvements to traditional retrievals were found using a variational method similar to the one presented here.

#### b. Rotated figure-four flight pattern

Figure 15 shows a 1.8-h rotated figure-four flight pattern (100-km radial legs) of the simulated Bonnie at 1-km height starting at 1200 UTC 23 August 1998 sampled by HIWRAP. This figure is intended to illustrate the spatial coverage of retrieval winds and reflectivity afforded by HIWRAP for the common rotated figure-four pattern executed during the NASA GRIP field experiment (Braun et al. 2013).

Table 1 presents a summary of the Cartesian velocity retrieval errors averaged over the HIWRAP sampling volume for this flight pattern. Results from three experiments with different random error perturbations added to the simulated Doppler velocities are shown:  $\pm 1$ –2 (ER1; default case),  $\pm 2$ –4 (ER2), and  $\pm 4$ –8  $\text{m s}^{-1}$  (ER3). Results from both the least squares and variational solutions are shown in Table 1.

For the default case, the systematic errors are  $-0.08$ ,  $0.04$ , and  $-0.11 \text{ m s}^{-1}$  for the zonal, meridional, and vertical wind components, respectively. A positive (negative) bias is where the retrievals are larger (smaller) than the model truth.

Table 1 shows that the low horizontal wind component errors are relatively robust to large random errors in the Doppler velocity. This is particularly true for the variational solutions. Increases of only  $\sim 1$  and  $0.60 \text{ m s}^{-1}$  in RMSE and  $\sim 4\%$  and  $2\%$  in REL for the least squares and variational solutions, respectively, are found for the horizontal wind components when adding the largest error perturbations ( $\pm 4$ –8  $\text{m s}^{-1}$ ). The vertical wind component is more sensitive to random errors. Although the RMSEs only increase by  $\sim 0.60$ – $0.75 \text{ m s}^{-1}$  for both retrieval methods when adding the largest error perturbations, this is significant as REL values increase by  $\sim 50\%$ – $75\%$ . The vertical velocity errors presented in Table 1 may seem large; this is due to averaging the errors over the entire radar sampling volume. However, as shown in Figs. 12 and 14b, there is strong across-track dependence on the vertical velocity errors. Therefore, if one focuses on the middle portion of the radar swath

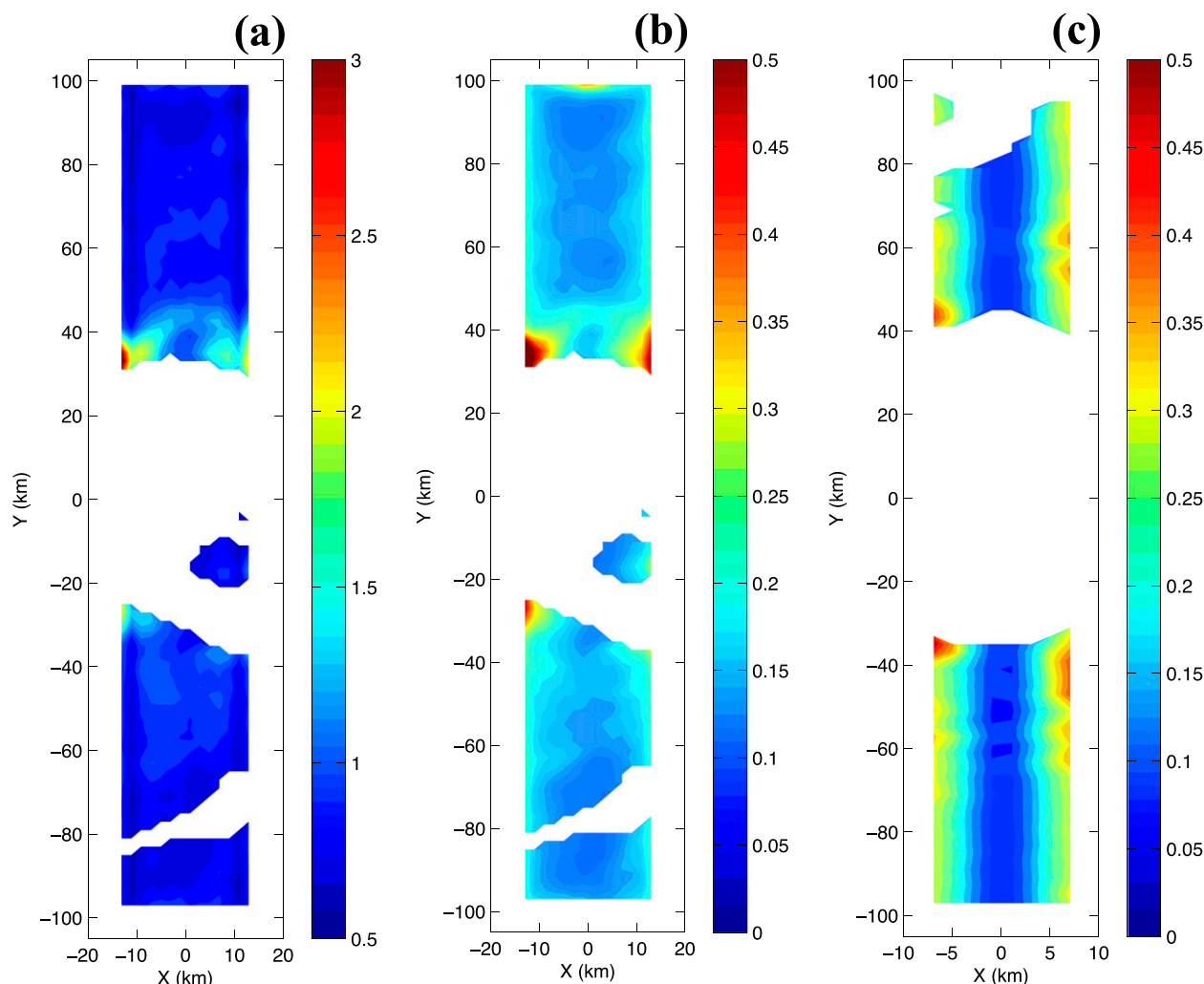


FIG. 13. Standard deviations of the Cartesian wind components using an error propagation analysis with least squares theory (see text for details). The figures are (a) zonal velocity at 1-km height, (b) meridional velocity at 1-km height, and (c) vertical velocity at 8-km height. Note the different x-axis scale for the vertical velocity figure.

(approximately  $\pm 5$  km from nadir), substantial reductions in vertical velocity errors can be achieved.

#### 4. Example wind retrievals from measured data

In this section, we illustrate the utility of the wind retrieval algorithms for analyzing hurricanes using measured data collected by IWRAP and HIWRAP. We first show least squares retrievals at nadir (simulated errors for the variational method are similar to the least squares at nadir; see Fig. 14) using IWRAP data collected in Hurricane Isabel (2003) 1900–1930 UTC 12 September. During this time period, Isabel was maintaining category 5 intensity with a minimum surface pressure of  $\sim 920$  hPa and maximum sustained winds of  $\sim 72 \text{ m s}^{-1}$  ( $\sim 160 \text{ mi h}^{-1}$ ).

Figure 16 shows a horizontal cross section ( $\sim 2$ -km height) of radar reflectivity (C band) in Hurricane Isabel at  $\sim 1900$  UTC 12 September 2003 from the lower fuselage radar on the NOAA P3 aircraft. There is a concentric eyewall present in Isabel at this time with an outer eyewall at a radius of  $\sim 60$  km from the storm center and an inner eyewall at  $\sim 30$ -km radius. The black arrow in Fig. 16 shows an outbound flight segment where the NOAA P3 aircraft (with IWRAP mounted underneath) penetrated the inner eyewall of Isabel and approached the outer eyewall.

Figure 17a shows a vertical cross section of IWRAP reflectivity at C band along the black arrow illustrated in Fig. 16. The IWRAP reflectivity is mapped to a grid with horizontal grid spacing of 0.25 km and vertical grid spacing of 30 m. The wind retrievals use this same grid

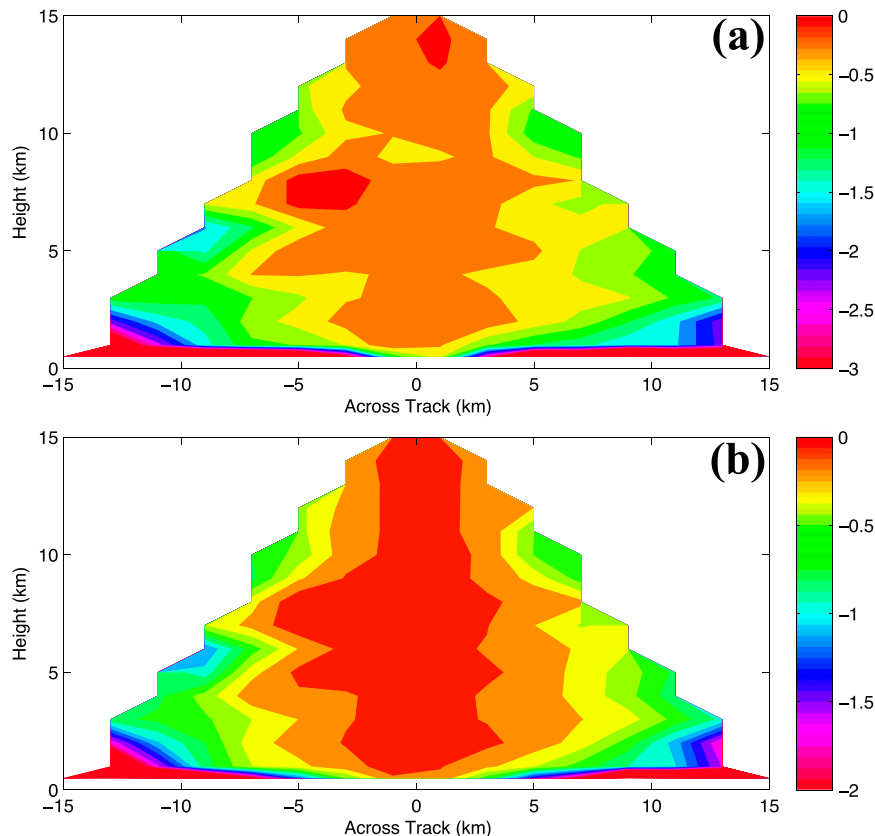


FIG. 14. Simulated HIWRAP retrieval RMSE differences (variational solution minus least squares solution) for (a) across-track velocity and (b) vertical velocity for the eyewall flight segment described in the text. In the RMSE calculation, the averages are taken in the along-track direction. In the figure negative values show where the variational solutions have lower RMSEs than the least squares method.

only the vertical grid spacing is set to 100 m. Data below  $\sim 0.40$ -km height is removed due to contamination by ocean surface scattering entering through the radar's main lobe. The inner eyewall of Isabel is centered at  $\sim 35$  km along track in Fig. 17a with peak reflectivities of  $\sim 50$  dBZ at C band. Reflectivity oscillations (bands of enhanced and depressed reflectivity) with wavelengths of  $\sim 2$ – $4$  km are located radially outside the inner eyewall of Isabel from  $\sim 40$  to 60 km along track.

Figure 17b shows the retrieved horizontal wind speeds at nadir using the C-band Doppler velocities (Nyquist interval of approximately  $\pm 225 \text{ m s}^{-1}$ ) with rain fall speeds calculated according to Ulbrich and Chilson (1994) and Heymsfield et al. (1999). Ulbrich and Chilson (1994) estimated the uncertainty in their rain fall speed relations due to particle size distribution variability at up to  $\sim 2 \text{ m s}^{-1}$ . These uncertainties have a small effect ( $< 0.1 \text{ m s}^{-1}$ ) on the horizontal wind retrievals but have a direct impact of up to  $2 \text{ m s}^{-1}$  on the vertical winds. For mixed-phase and some ice particles (not shown in this

paper), the uncertainties are generally larger and will have a larger effect on the vertical wind retrievals. To address noise in the data and calculations, Doppler velocities with pulse-pair correlation coefficient (PPCC) values below 0.25 were removed and  $\beta$  in Eq. (3) was increased to 7. The inner eyewall of Isabel is intense with maximum wind speeds of  $\sim 80 \text{ m s}^{-1}$  and average values of  $65$ – $70 \text{ m s}^{-1}$ . Radially outside the inner eyewall, oscillations in the wind speeds are consistent with the reflectivity structure in Fig. 17a.

Figure 17c shows the retrieved vertical winds at nadir with the same data processing and quality control as the horizontal winds. The core of the inner eyewall (centered at 35 km along track) is dominated by a broad region of downward motion with maximum values between approximately  $-3$  and  $-5 \text{ m s}^{-1}$ . A strong updraft sloping radially outward with height is located on the inner edge of the primary eyewall with values between 5 and  $15 \text{ m s}^{-1}$ . The hurricane structure is consistent with a concentric eyewall cycle (e.g., Willoughby et al. 1982)



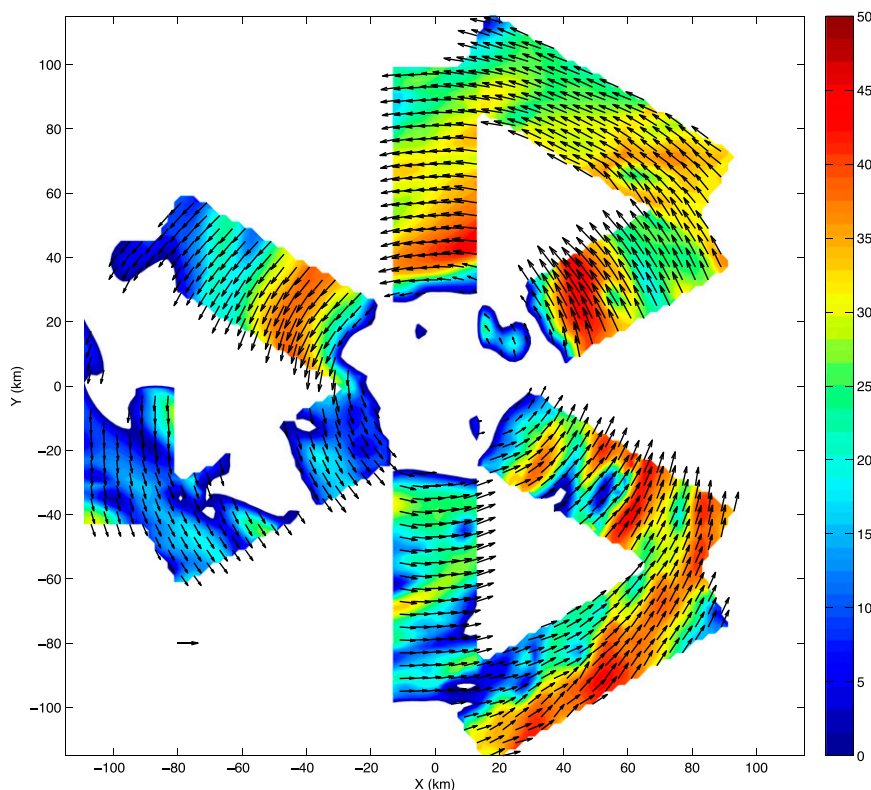


FIG. 15. HIWRAP 1.8-h rotated figure-four sampling of the Bonnie numerical simulation at 1-km height starting at 1200 UTC 23 Aug 1998. The shading is simulated reflectivity (dBZ) and the reference arrow at  $(-80, -80)$  is  $50 \text{ m s}^{-1}$ . The large hole (no reflectivity/winds) in the center is the large eye of the simulated Bonnie.

occurring within Isabel at this time. In the region between the inner and outer eyewalls ( $\sim 40$ – $60$  km along track), there are oscillations in vertical velocity that are well correlated with the oscillations in the reflectivity structure shown in Fig. 17a. This suggests some type of wave is propagating radially outward away from the inner eyewall and toward the outer eyewall.

The horizontal and vertical wind speed estimates from the IWRAP retrievals match well with flight-level measurements from the NOAA N42 aircraft. To make these

comparisons, the 1-Hz flight-level winds are interpolated to the IWRAP analysis grid ( $0.25$  km in the along-track direction) and plotted on top of the IWRAP retrievals at nadir. The first useful gate of IWRAP data was  $\sim 100$ – $130$  m below the N42 aircraft.

Figure 18a shows comparisons of the horizontal wind speeds, revealing that the IWRAP retrievals are able to recover the peak values of  $\sim 75$ – $80 \text{ m s}^{-1}$  well in addition to the very turbulent structure. As shown in Fig. 17, the eyewall of Isabel is tilted radially outward with height,

TABLE 1. Summary of HIWRAP velocity retrieval errors for the Hurricane Bonnie (1998) simulated 1.8-h rotated figure-four flight pattern shown in Fig. 15. See text for details. In the experiment name column below, the subscripts “ $L$ ” and “ $V$ ” stand for the least squares and variational solutions, respectively. The RMSEs ( $\text{m s}^{-1}$ ) and the RELs (% , rounded to the nearest whole number) are given. The variable  $R$  is the correlation coefficient.

Expt name	Zonal			Meridional			Vertical		
	RMSE	REL	$R$	RMSE	REL	$R$	RMSE	REL	$R$
ER1 <sub>L</sub>	1.99	8	0.99	2.64	10	0.99	1.73	169	0.44
ER1 <sub>V</sub>	1.61	7	0.99	2.12	8	0.99	1.38	129	0.53
ER2 <sub>L</sub>	2.20	9	0.99	2.87	11	0.99	1.90	185	0.41
ER2 <sub>V</sub>	1.74	7	0.99	2.28	8	0.99	1.52	140	0.50
ER3 <sub>L</sub>	2.88	12	0.99	3.64	14	0.99	2.47	236	0.33
ER3 <sub>V</sub>	2.20	9	0.99	2.82	10	0.99	1.98	178	0.41

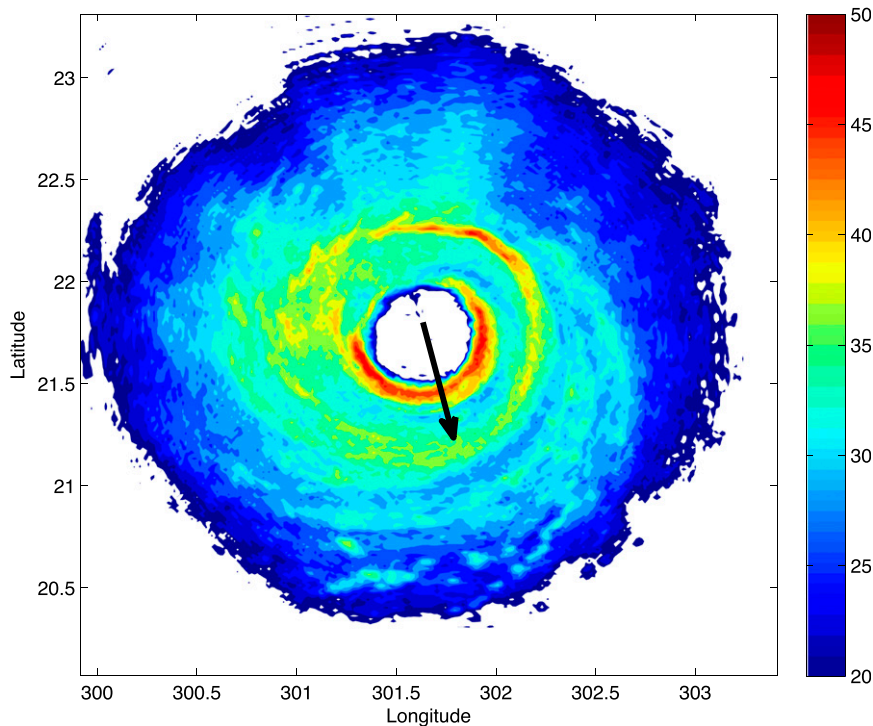


FIG. 16. Horizontal cross section ( $\sim 2$ -km height) of radar reflectivity (C band) in Hurricane Isabel at  $\sim 1900$  UTC 12 Sep 2003 from the lower fuselage radar on the NOAA P3 aircraft. The black arrow denotes a NOAA P3 flight segment where IWRAP data are analyzed.

which is evident in Fig. 18a (e.g., see between 30 and 35 km along track) because of the height difference between the flight-level measurements and the IWRAP retrievals. The low bias in retrieved horizontal wind speed observed in Fig. 18a is probably due to this height difference. Shifting the IWRAP retrievals by one along-track grid point ( $0.25$  km) to account for the eyewall tilt results in an RMSE of  $4.1 \text{ m s}^{-1}$  (REL of 7%) and a correlation coefficient of 0.94. Figure 18b shows the vertical wind speed comparisons with the large peak updrafts of  $\sim 12 \text{ m s}^{-1}$  and turbulent structure observed in the flight-level data resolved well by the IWRAP retrievals. Applying the same  $0.25$ -km along-track shift to the retrievals results in an RMSE of  $2.0 \text{ m s}^{-1}$  (REL of 59%) and an excellent correlation coefficient of 0.87. Of course, these statistics only represent one flight line and additional comparisons including those more closely aligned in height are needed.

We now illustrate retrievals of the horizontal wind vector using the variational method for HIWRAP observations of Tropical Storm Matthew (2010) during the NASA GRIP field experiment. The constraint weights are the same as those used for the simulated data except for the Laplacian smoothing term, which had a value of  $0.5\Delta x^4$ . Figure 19 shows a Geostationary Operational Environmental Satellite (GOES) infrared image of

Matthew at 0645 UTC 24 September 2010 overlaid with the GH track. During this time period, Matthew was a weak tropical storm with a minimum surface pressure of 1003 hPa and maximum sustained winds of  $\sim 23 \text{ m s}^{-1}$  with vertical wind shear from the northeast at  $10$ – $15 \text{ m s}^{-1}$ . Despite the significant vertical wind shear, Matthew was intensifying steadily with convective bursts (shown by the brightness temperatures between 185 and 190 K in Fig. 19) located in the downshear portions of the storm. The blue highlighted lines in Fig. 19 denote the HIWRAP flight segments analyzed.

Figure 20 shows retrievals of the horizontal wind vector overlaid on Ku-band reflectivity at 3-km height for the three blue flight segments highlighted in Fig. 19 between 0552 and 0742 UTC 24 September 2010. The retrieval grid is Lagrangian, following the National Hurricane Center (NHC) estimate of the center of Matthew at the middle of each flight segment, with a grid spacing of 1 km. The swath width of HIWRAP at 3-km height is  $\sim 26$  km. Overlaps in the three passes are simply averaged together.

The GRIP experiment was the first time HIWRAP collected significant data and some issues with the data (e.g., excessive noise and problems with dealiasing Doppler velocities) were found. To address these issues, we have done two things: 1) pulse-pair estimates

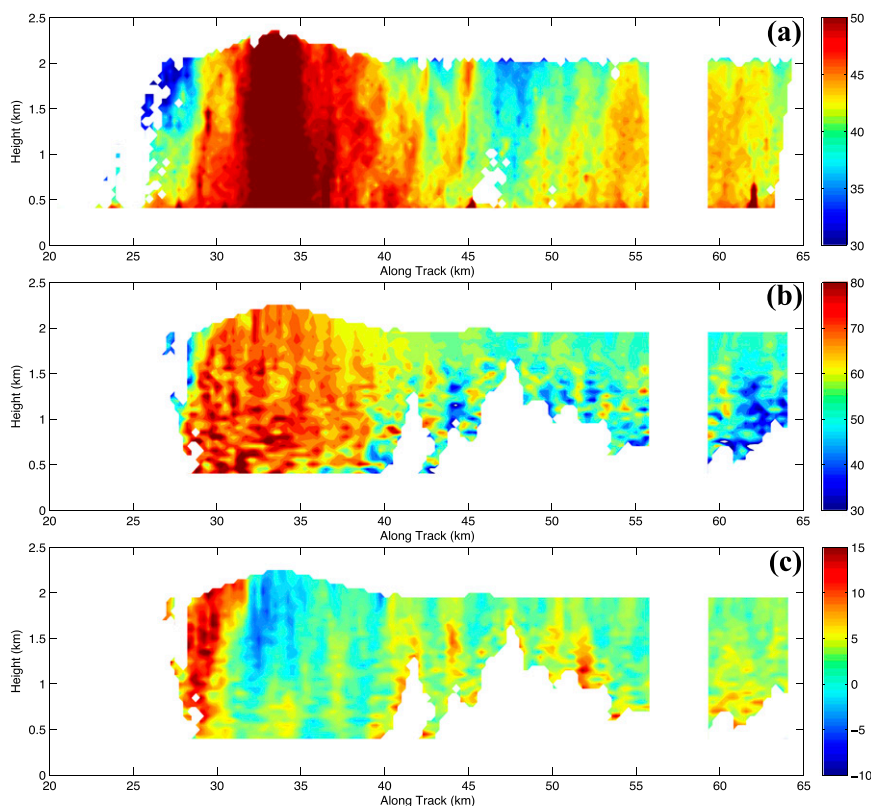


FIG. 17. Vertical cross section of IWRAP data at nadir in Hurricane Isabel 1900–1910 UTC 12 Sep 2003 along the flight segment shown by the black arrow in Fig. 16. The data shown are (a) C-band reflectivity (dBZ), (b) retrieved horizontal wind speeds ( $\text{m s}^{-1}$ ), and (c) retrieved vertical wind speeds ( $\text{m s}^{-1}$ ). The vertical axis is exaggerated to show detail.

were reprocessed with 128 pulses averaged (azimuthal resolution of  $\sim 2.8^\circ$ ), which improves the signal-to-noise ratio as well as the performance of the dual-PRF dealiasing calculation; and 2) Doppler velocities below the noise saturation threshold (determined using a power threshold, which translates to  $\sim 25$  dBZ at 3-km height) were removed. The term  $\beta$  in Eq. (3) was set to 6 everywhere. Hydrometeor fall speeds are removed from the data using the rain relations described in Ulbrich and Chilson (1994) and Heymsfield et al. (1999).

A cyclonic flow is evident in Fig. 20 despite the gaps in data, which are most pronounced to the northeast of the “X” due to vertical wind shear displacing most of the precipitating convection to the downshear quadrants of the storm. Although no wind observations are currently available in the northeast portion of the storm (ocean surface wind retrievals for HIWRAP are currently being designed), passive microwave satellite images of Matthew (not shown) within the time frame of Fig. 20 reveal curved bands in this section, indicating a continuation of the cyclonic flow defined by the HIWRAP retrievals.

The estimated center of this cyclonic flow is  $\sim 50$  km west to northwest of the center estimate from the NHC at  $x \sim -45$  km,  $y \sim 23$  km. The strongest winds of  $25\text{--}35 \text{ m s}^{-1}$  are located to the north of the HIWRAP-derived cyclonic flow center coincident with deep convective towers. Deep convective towers are also present to the southwest of the HIWRAP center, embedded within the partial eyewall shown by the strong reflectivity gradients and curved flow ( $x \sim -70$  km,  $y \sim 0$  km). The wind speeds in this section are  $\sim 10 \text{ m s}^{-1}$  on average with stronger winds of  $15\text{--}20 \text{ m s}^{-1}$  connected with the deep convection (high reflectivity regions).

Figure 21 shows the standard deviations in the wind speeds (described in section 2b) for the HIWRAP composite analysis shown in Fig. 20. The standard deviations are computed by taking the square root of the diagonal elements of  $\delta \mathbf{g}^2$  in Eq. (10). This produces a standard deviation for each wind component, and we have taken the magnitude of the horizontal standard deviations to summarize the errors in the horizontal winds. The theoretical wind speed errors are the smallest ( $\sim 0.5 \text{ m s}^{-1}$ ) in the middle section of each swath and

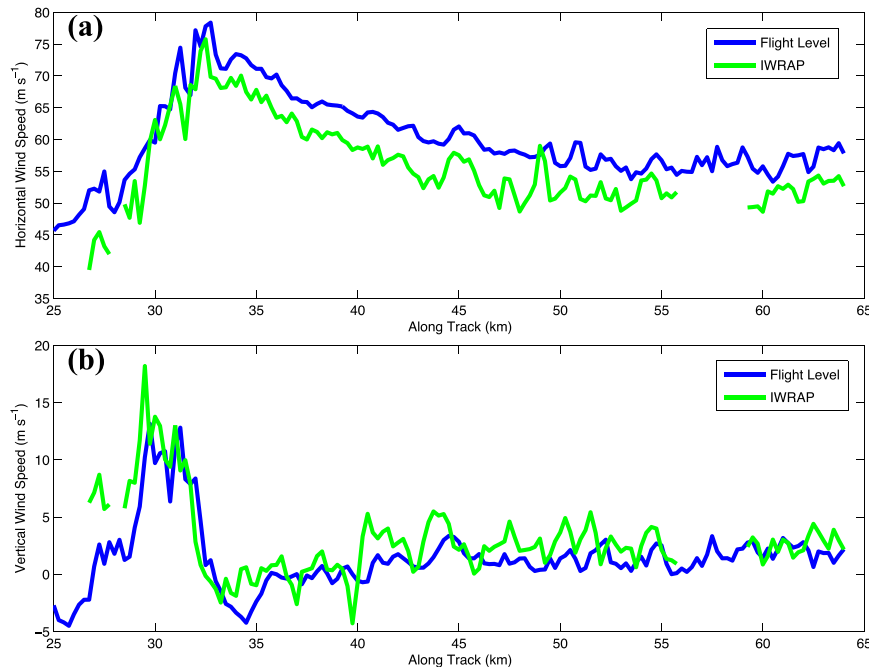


FIG. 18. Comparison of flight-level measurements and IWRAP retrievals for (a) horizontal wind speeds and (b) vertical wind speeds. The IWRAP retrievals are  $\sim 100$ – $130$  m lower in altitude than the flight-level winds. See text for details.

increase toward the swath edges ( $\sim 1$ – $2$   $\text{m s}^{-1}$ ). These results are consistent with the error analysis described in section 3. The largest errors of  $\sim 3$ – $5$   $\text{m s}^{-1}$  occur in the northern section of the analysis (especially along the edges), where the wind speeds are strongest. These errors, derived from a propagation analysis, are useful for providing an estimate of the errors in the computed winds by taking into account the radar geometry and quality of the least squares fit to the observations.

## 5. Summary and conclusions

In this paper, algorithms for the retrieval of atmospheric winds in precipitating systems from downward-pointing, conically scanning airborne Doppler radars were presented with a focus on the IWRAP and HIWRAP systems. Retrievals of the three Cartesian wind components over the entire radar sampling volume are described, which can be determined using either a traditional least squares or a variational solution procedure.

The random errors in the retrievals due to the airborne radar geometry and noise in the Doppler velocities are evaluated using both an error propagation analysis with least squares theory and a numerical simulation of a hurricane. These error analyses show that the along-track and vertical wind RMSEs have strong across-track dependence with values of  $\sim 0.25$   $\text{m s}^{-1}$  at nadir to  $\sim 1.00$  and  $\sim 2.00$   $\text{m s}^{-1}$  at the swath edges,

respectively. The across-track wind errors have a more complicated distribution, but in general they get larger at the swath edges, which is due to the radar viewing geometry becoming collinear along the swath edges. On average, the across-track wind errors are  $\sim 2.50$   $\text{m s}^{-1}$  or

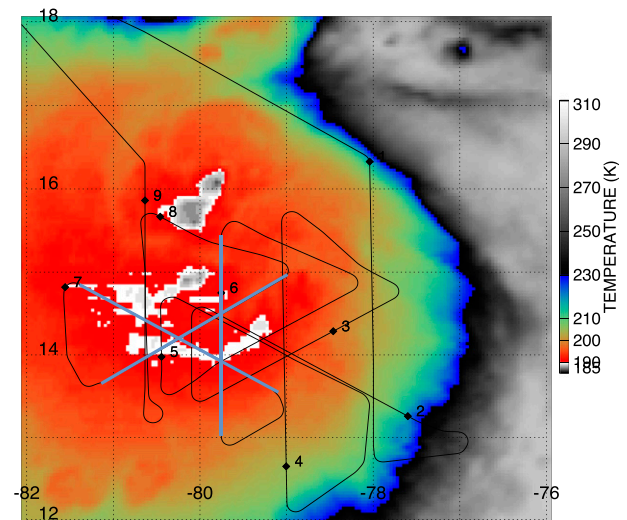


FIG. 19. GOES infrared image of Tropical Storm Matthew (2010) at 0645 UTC 24 Sep 2010 overlaid with the GH track during the NASA GRIP field experiment. The numbers on the track indicate the hour (UTC) on 24 Sep 2010. The blue lines overlaid on the track highlight the HIWRAP overpasses analyzed.



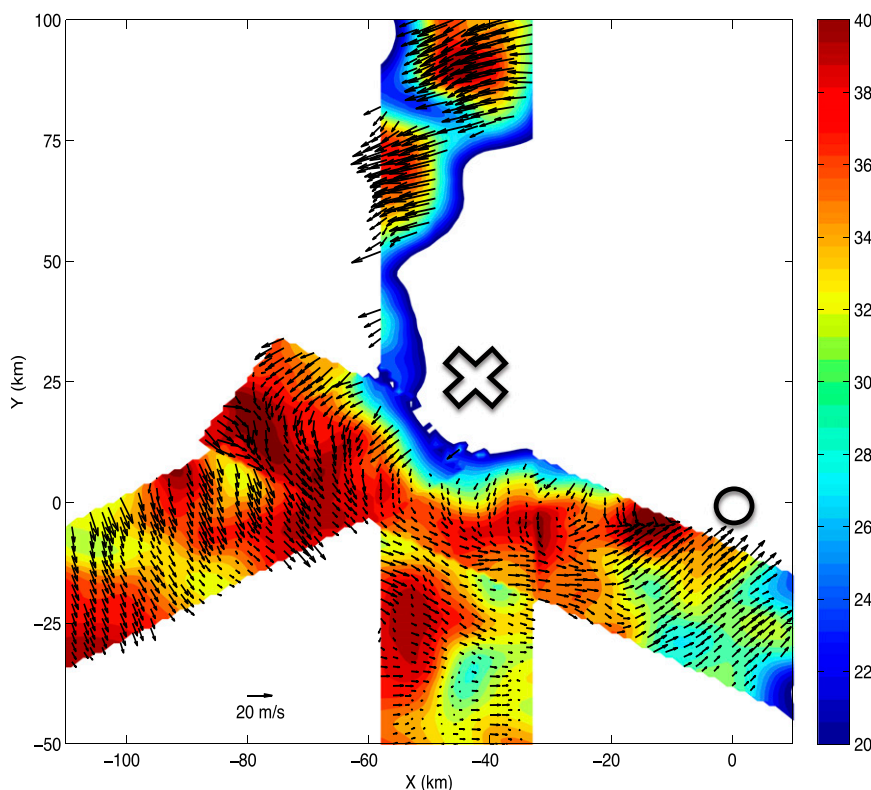


FIG. 20. HIWRAP horizontal wind vector retrievals overlaid on Ku-band reflectivity for the three Matthew overpasses highlighted in Fig. 19. See text for details. The center of Matthew's circulation as defined by HIWRAP is shown by the "X," and the NHC's center estimate is shown by the "O."

7% of the local wind speed. For typical rotated figure-four flight patterns through hurricanes, the zonal and meridional wind speed errors are  $\sim 1.5\text{--}2.0\text{ m s}^{-1}$  or 7%–8% of the local wind speed when adding in  $\pm 1\text{--}2\text{ m s}^{-1}$  of random noise to the simulated Doppler velocities.

Comparisons of IWRAP-measured data retrievals at nadir to flight-level data show errors of  $\sim 2.0\text{ m s}^{-1}$  for vertical winds and  $\sim 4.0\text{ m s}^{-1}$  for horizontal wind speed ( $\sim 7\%$  of the hurricane wind speed). Additional sources of error, such as hydrometeor fall speed uncertainties and a small height offset in the comparisons, are likely responsible for the larger vertical wind errors when compared to the simulated error analyses.

Evaluations of the least squares and variational solutions showed that the variational method was able to reduce the volume-averaged vertical and across-track wind speed errors by  $\sim 0.50$  and  $0.80\text{ m s}^{-1}$ , respectively. The zonal and meridional wind speed errors from the rotated figure-four flight pattern were also reduced with the variational method. This improvement occurs at the swath edges and at the lowest analysis levels through the anelastic mass continuity constraint coupled with the impermeability condition. Little improvement was found

for the along-track velocity because the least squares errors were already very low.

For the least squares method, one of the unique positive attributes is the ability to analyze the theoretical uncertainties in the wind components through an error propagation analysis, which was derived and illustrated in this study. One unique drawback of the least squares method is the potential introduction of significant errors in the wind field when applying some dynamic constraints, such as the conservation of mass, because of problems associated with explicit integration techniques (Gao et al. 1999; Potvin et al. 2012). The variational solution procedure eliminates these problems by evaluating (rather than integrating) the dynamic constraints simultaneously, which removes boundary and accumulation errors that plague explicit integrations. The results in this study show that the variational method is generally preferable to the least squares method for the IWRAP/HIWRAP geometry, which is consistent with previous ground-based studies (Gao et al. 1999; Potvin et al. 2012). However, there are drawbacks of the variational method such as difficulties determining the optimal weights for the dynamic constraints and increased

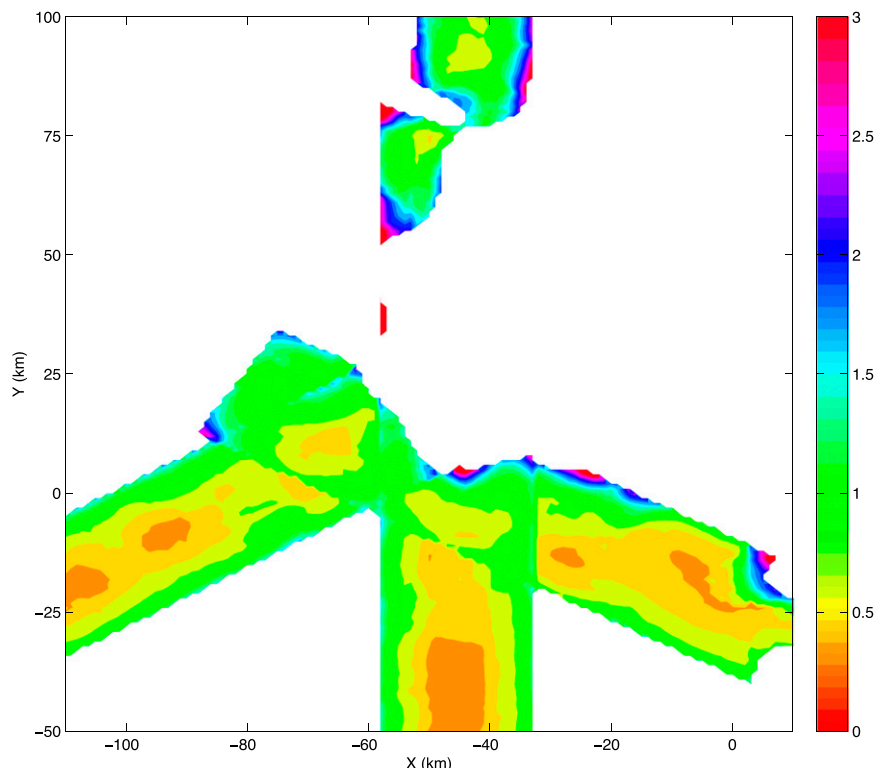


FIG. 21. Standard deviations in the horizontal wind speeds for the HIWRAP analysis shown in Fig. 20. The standard deviations are computed by taking the square root of the diagonal elements of  $\delta \mathbf{g}^2$  in Eq. (10). This produces a standard deviation for each wind component, so we have taken the magnitude of the horizontal standard deviations to summarize the errors in the horizontal winds.

computer time relative to the least squares method that are important for real-time applications.

A major science motivation for the IWRAP and HIWRAP airborne radars is the study of hurricanes. Examples of measured data wind retrievals from IWRAP during an eyewall replacement cycle in Hurricane Isabel (2003) and from HIWRAP during the development of Tropical Storm Matthew (2010) were shown. These high-resolution measurements, especially for IWRAP, along with the dual-frequency nature of both radars (useful for characterizing the particle size distribution in future work) and the long sampling times of HIWRAP from the NASA Global Hawk aircraft provide a unique ability to address important hurricane science questions. A detailed science analysis of the IWRAP and HIWRAP data associated with these wind retrieval examples is warranted and will be reported in a forthcoming paper.

**Acknowledgments.** We thank Matt McLinden for his feedback on the HIWRAP data as well as his engineering efforts. We also thank Dr. Lihua Li, Martin Perrine, Jaime Cervantes, and Ed Zenker for their engineering

work with the HIWRAP radar. We thank the University of Massachusetts Amherst Microwave Remote Sensing Laboratory for its engineering efforts. Thanks also to Dr. Jim Carswell for discussions and support of the IWRAP work. The first author thanks Dr. Anthony Didlake for his comments on the retrieval algorithms. The majority of this research was carried out when the first author was a postdoctoral fellow through the NASA Postdoctoral Program (NPP) stationed at Goddard Space Flight Center. Steve Guimond thanks NPP for its support of this work. Finally, we thank three anonymous reviewers for their helpful comments and constructive criticism.

#### REFERENCES

- Armijo, L., 1969: A theory for the determination of wind and precipitation velocities with Doppler radars. *J. Atmos. Sci.*, **26**, 570–575, doi:10.1175/1520-0469(1969)026<0570:ATFTDO>2.0.CO;2.
- Bell, M. M., M. T. Montgomery, and K. A. Emanuel, 2012: Air–sea enthalpy and momentum exchange at major hurricane wind speeds observed during CBLAST. *J. Atmos. Sci.*, **69**, 3197–3222, doi:10.1175/JAS-D-11-0276.1.



- Bohne, A. R., and R. C. Srivastava, 1976: Random errors in wind and precipitation fall speed measurements by a triple Doppler radar system. Preprints, *17th Conf. on Radar Meteorology*, Seattle, WA, Amer. Meteor. Soc., 7–14.
- Braun, S., M. Montgomery, and Z. Pu, 2006: High-resolution simulation of Hurricane Bonnie (1998). Part I: The organization of eyewall vertical motion. *J. Atmos. Sci.*, **63**, 19–42, doi:10.1175/JAS3598.1.
- , and Coauthors, 2013: NASA's Genesis and Rapid Intensification Processes (GRIP) field experiment. *Bull. Amer. Meteor. Soc.*, **94**, 345–363, doi:10.1175/BAMS-D-11-00232.1.
- Chong, M., and C. Campos, 1996: Extended overdetermined dual-Doppler formalism in synthesizing airborne Doppler radar data. *J. Atmos. Oceanic Technol.*, **13**, 581–597, doi:10.1175/1520-0426(1996)013<0581:EODDFI>2.0.CO;2.
- Doviak, R. J., and D. S. Zrnić, 1993: *Doppler Radar and Weather Observations*. Academic Press, 562 pp.
- Fernandez, D. E., E. Kerr, A. Castells, S. Frasier, J. Carswell, P. S. Chang, P. Black, and F. Marks, 2005: IWRAP: The Imaging Wind and Rain Airborne Profiler for remote sensing of the ocean and the atmospheric boundary layer within tropical cyclones. *IEEE Trans. Geosci. Remote Sens.*, **43**, 1775–1787, doi:10.1109/TGRS.2005.851640.
- Gamache, J. F., F. D. Marks, and F. Roux, 1995: Comparison of three airborne Doppler sampling techniques with airborne in situ wind observations in Hurricane Gustav (1990). *J. Atmos. Oceanic Technol.*, **12**, 171–181, doi:10.1175/1520-0426(1995)012<0171:COTADS>2.0.CO;2.
- Gao, J., M. Xue, A. Shapiro, and K. K. Droegemeier, 1999: A variational method for the analysis of three-dimensional wind fields from two Doppler radars. *Mon. Wea. Rev.*, **127**, 2128–2142, doi:10.1175/1520-0493(1999)127<2128:AVMFTA>2.0.CO;2.
- Heymsfield, G. M., 1976: Statistical objective analysis of dual-Doppler radar data from a tornadic storm. *J. Appl. Meteor.*, **15**, 59–68, doi:10.1175/1520-0450(1976)015<0059:SOAODD>2.0.CO;2.
- , and Coauthors, 1996: The EDOP radar system on the high-altitude NASA ER-2 aircraft. *J. Atmos. Oceanic Technol.*, **13**, 795–809, doi:10.1175/1520-0426(1996)013<0795:TERSOT>2.0.CO;2.
- , J. B. Halverson, and I. J. Caylor, 1999: A wintertime Gulf Coast squall line observed by EDOP airborne Doppler radar. *Mon. Wea. Rev.*, **127**, 2928–2950, doi:10.1175/1520-0493(1999)127<2928:AWGCSL>2.0.CO;2.
- Hildebrand, P. H., and Coauthors, 1996: The ELDORA/ASTRAIA airborne Doppler weather radar: High-resolution observations from TOGA COARE. *Bull. Amer. Meteor. Soc.*, **77**, 213–233, doi:10.1175/1520-0477(1996)077<0213:TEADWR>2.0.CO;2.
- Klimowski, B. A., and J. D. Marwitz, 1992: The synthetic dual-Doppler analysis technique. *J. Atmos. Oceanic Technol.*, **9**, 728–745, doi:10.1175/1520-0426(1992)009<0728:TSDDAT>2.0.CO;2.
- Koch, S. E., M. desJardins, and P. J. Kocin, 1983: An interactive Barnes objective map analysis scheme for use with satellite and conventional data. *J. Climate Appl. Meteor.*, **22**, 1487–1503, doi:10.1175/1520-0450(1983)022<1487:AIBOMA>2.0.CO;2.
- Lee, W. C., P. Dodge, F. D. Marks Jr., and P. H. Hildebrand, 1994: Mapping of airborne Doppler radar data. *J. Atmos. Oceanic Technol.*, **11**, 572–578, doi:10.1175/1520-0426(1994)011<0572:MOADRD>2.0.CO;2.
- Lhermitte, R. M., 1970: Dual-Doppler radar observations of convective storm circulation. Preprints, *14th Radar Meteorology Conf.*, Tucson, AZ, Amer. Meteor. Soc., 139–144.
- Li, L., G. M. Heymsfield, J. Carswell, D. Schaubert, J. Creticos, and M. Vega, 2008: High-Altitude Imaging Wind and Rain Airborne Radar (HIWRAP). *2008 IEEE International Geoscience and Remote Sensing Symposium: Proceedings*, IEEE, III-354–III-357, doi:10.1109/IGARSS.2008.4779356.
- López-Carrillo, C., and D. J. Raymond, 2011: Retrieval of three-dimensional wind fields from Doppler radar data using an efficient two-step approach. *Atmos. Meas. Tech.*, **4**, 2717–2733, doi:10.5194/amt-4-2717-2011.
- Marks, F. D., and R. A. Houze, 1984: Airborne Doppler radar observations in Hurricane Debby. *Bull. Amer. Meteor. Soc.*, **65**, 569–582, doi:10.1175/1520-0477(1984)065<0569:ADROIH>2.0.CO;2.
- , —, and J. Gamache, 1992: Dual-aircraft investigation of the inner core of Hurricane Norbert: Part I: Kinematic structure. *J. Atmos. Sci.*, **49**, 919–942, doi:10.1175/1520-0469(1992)049<0919:DAIOTI>2.0.CO;2.
- Matejka, T., and D. L. Bartels, 1998: The accuracy of vertical air velocities from Doppler radar data. *Mon. Wea. Rev.*, **126**, 92–117, doi:10.1175/1520-0493(1998)126<0092:TAOVAV>2.0.CO;2.
- Potvin, C. K., D. Betten, L. J. Wicker, K. L. Elmore, and M. I. Biggerstaff, 2012: 3DVAR versus traditional dual-Doppler wind retrievals of a simulated supercell thunderstorm. *Mon. Wea. Rev.*, **140**, 3487–3494, doi:10.1175/MWR-D-12-00063.1.
- Ray, P. S., K. K. Wagner, K. W. Johnson, J. J. Stephens, W. C. Baumgarner, and E. A. Mueller, 1978: Triple-Doppler observations of a convective storm. *J. Appl. Meteor.*, **17**, 1201–1212, doi:10.1175/1520-0450(1978)017<1201:TDOOAC>2.0.CO;2.
- , C. L. Ziegler, W. Bumgarner, and R. J. Serafin, 1980: Single- and multiple- Doppler radar observations of tornadic storms. *Mon. Wea. Rev.*, **108**, 1607–1625, doi:10.1175/1520-0493(1980)108<1607:SAMDRO>2.0.CO;2.
- Reasor, P. D., M. D. Eastin, and J. F. Gamache, 2009: Rapidly intensifying Hurricane Guillermo (1997). Part I: Low-wavenumber structure and evolution. *Mon. Wea. Rev.*, **137**, 603–631, doi:10.1175/2008MWR2487.1.
- Sasaki, Y., 1970: Some basic formalisms in numerical variational analysis. *Mon. Wea. Rev.*, **98**, 875–883, doi:10.1175/1520-0493(1970)098<0875:SBFINV>2.3.CO;2.
- Shanno, D. F., 1978: Conjugate gradient methods with inexact searches. *Math. Oper. Res.*, **3**, 244–256, doi:10.1287/moor.3.3.244.
- , and K. H. Phua, 1980: Remark on “Algorithm 500: Minimization of Unconstrained Multivariate Functions [E4].” *ACM Trans. Math. Software*, **6**, 618–622, doi:10.1145/355921.355933.
- Shapiro, A., C. K. Potvin, and J. Gao, 2009: Use of a vertical vorticity equation in variational dual-Doppler wind analysis. *J. Atmos. Oceanic Technol.*, **26**, 2089–2106, doi:10.1175/2009JTECHA1256.1.
- Strang, G., 1986: *Introduction to Applied Mathematics*. Wellesley-Cambridge Press, 758 pp.
- Tian, L., G. Heymsfield, S. Guimond, L. Li, and R. Srivastava, 2011: 3D wind retrieval from downward conical scanning airborne Doppler radar. Preprints, *35th Conf. on Radar Meteorology*, Pittsburgh, PA, Amer. Meteor. Soc., P3.37. [Available online at <https://ams.confex.com/ams/35Radar/webprogram/Paper191878.html>.]
- Ulbrich, C. W., and P. B. Chilson, 1994: Effects of variations in precipitation size distribution and fallspeed law parameters on relations between mean Doppler

- fallspeed and reflectivity factor. *J. Atmos. Oceanic Technol.*, **11**, 1656–1663, doi:10.1175/1520-0426(1994)011<1656:EOVIPS>2.0.CO;2.
- Willoughby, H. E., J. A. Clos, and M. G. Shoreibah, 1982: Concentric eyewalls, secondary wind maxima, and the evolution of the hurricane vortex. *J. Atmos. Sci.*, **39**, 395–411, doi:10.1175/1520-0469(1982)039<0395:CEWSWM>2.0.CO;2.
- Yang, S., and Q. Xu, 1996: Statistical errors in variational data assimilation—A theoretical one-dimensional analysis applied to Doppler wind retrieval. *J. Atmos. Sci.*, **53**, 2563–2577, doi:10.1175/1520-0469(1996)053<2563:SEIVDA>2.0.CO;2.
- Ziegler, C. L., 1978: A dual Doppler variational objective analysis as applied to studies of convective storms. M.S. thesis, Dept. of Meteorology, University of Oklahoma, 115 pp.